

# Modeling of Organic Light Emitting Diodes: From Molecular to Device Properties

Pascal Kordt,\* Jeroen J. M. van der Holst, Mustapha Al Helwi, Wolfgang Kowalsky, Falk May, Alexander Badinski, Christian Lennartz, and Denis Andrienko\*

The progress in modeling of charge transport in disordered organic semiconductors on various length scales, from atomistic to macroscopic, is reviewed. This includes evaluation of charge transfer rates from first principles, parametrization of coarse-grained lattice and off-lattice models, and solving the master and drift-diffusion equations. Special attention is paid to linking the length scales and improving the efficiency of the methods. All techniques are illustrated on an amorphous organic semiconductor, DPBIC, a hole conductor and electron blocker used in state of the art organic light emitting diodes (OLEDs). The outlined multiscale scheme can be used to predict OLED properties without fitting parameters, starting from chemical structures of compounds.

## 1. Introduction

The discovery of electrical conductivity in conjugated polymers<sup>[1]</sup> has marked the birth of the field of organic semiconductors, providing a new class of materials suitable for manufacturing of field effect transistors,<sup>[2]</sup> light emitting diodes,<sup>[3]</sup> and photovoltaic cells.<sup>[4]</sup> Cost-efficiency, enhanced processability, and chemical tunability have immediately been recognized as distinct properties of organic semiconductors.<sup>[5–8]</sup> Since then, organic light emitting diodes (OLEDs) have been incorporated into active-matrix displays and nowadays are produced on an industrial scale.<sup>[3,9]</sup> At the same time, white OLEDs are considered as promising candidates for lighting applications.<sup>[9,10]</sup>

In spite of this progress, there is still a need to improve lifetimes and efficiencies, especially of blue phosphorescent OLEDs, a task which requires designing new materials and optimizing device architectures. This is, of course, impossible

without understanding elementary processes occurring in a device. In a phosphorescent OLED, schematically shown in **Figure 1**, electrons and holes are injected into the transport layers, which ensure their balanced delivery to the emission layer (EML). To allow for triplet-harvesting mediated by spin-orbit coupling, the EML consists of an organic semiconductor (host) doped by a transition-metal coordinated compound, the emitter (guest). The excitation of the emitter can be achieved either by an energy transfer process, i.e., by the formation of an exciton on a host molecule with subsequent energy transfer

to the dopant, or by a direct charge transfer process. In the latter case, one of the charge carriers is trapped on the emitter and attracts a charge of opposite sign, forming a neutral on-site exciton. Hence, an interplay between the hole, electron, and exciton mobilities, relative energy offsets, energetic disorder, and recombination rates determines the charge/exciton profiles in a device and therefore its current–voltage–luminescence characteristics. In principle, it is possible to reconstruct these profiles by using charge-transport and exciton-transport models and fitting the experimental current–voltage curves.<sup>[11–13]</sup> This approach, however, does not provide a link to the chemical composition or morphological order and hence does not allow to prescreen organic compounds prior to their synthesis.

In this situation, computer simulations can help by linking device efficiency to the morphological order and molecular structures. A frequently used ansatz incorporates simulations of atomistic morphologies using classical force-fields, evaluation of charge/exciton transfer rates with first principles methods, and a subsequent analysis of the solution of the master equation.<sup>[14–23]</sup> This microscopic model is, however, computationally demanding: a layer of a few hundred nanometers thickness requires simulation boxes of  $\sim 10^7$  atoms, even if periodic boundary conditions are used in the directions perpendicular to the applied field.

To remedy the situation, extensions to this scheme have been proposed, as depicted in **Figure 2**. The most straightforward solution is to parametrize a lattice model by matching certain macroscopic properties of the atomistic and lattice models. For example, if charge carrier mobility is the property of interest, one can use the parametric dependencies provided by the family of Gaussian disorder models (GDM).<sup>[24–28]</sup> Note that a similar approach is often employed to interpret experimental data, i.e., to fit the measured mobility as a function of applied field, charge carrier density, and temperature.

P. Kordt, Dr. J. J. M. van der Holst, Dr. D. Andrienko  
Max Planck Institute for Polymer Research  
Ackermannweg 10,  
55128 Mainz, Germany  
E-mail: kordt@mpip-mainz.mpg.de;  
denis.andrienko@mpip-mainz.mpg.de

Dr. M. Al Helwi, Dr. F. May, Dr. C. Lennartz  
BASF SE, GVE/M-B009  
67056 Ludwigshafen, Germany  
Dr. M. Al Helwi, Prof. W. Kowalsky  
IHF Institut  
Technische Universität Braunschweig  
Brunswick, Germany

Dr. A. Badinski  
BASF SE, GVM/S-B009  
67056 Ludwigshafen, Germany



DOI: 10.1002/adfm.201403004

In our case, simulated instead of experimentally measured mobility values are used. This strategy, however, has two significant drawbacks. First, it relies on approximations made to construct the underlying models, which may not hold for the system of interest. Second, the model parametrization is usually performed in stationary conditions. It is therefore not immediately obvious that the same model can be used to describe nonequilibrium (transient) properties of the system. An alternative approach is to construct an off-lattice model by matching mesoscopic system properties, such as distributions of molecular positions and orientations, electronic couplings, and site energies.<sup>[29,30]</sup> Once parametrized, this model will not require explicit simulations of atomistic morphologies and quantum-chemical evaluations of rates and can therefore be used to simulate large systems.

In this Feature Article we illustrate both approaches on an amorphous phase of DPBIC, the chemical structure of which is shown in Figure 1, a compound used in hole-conducting and electron-blocking layers in blue phosphorescent OLEDs.<sup>[21,31]</sup> In particular, we show how material properties such as density, radial distribution functions, ionization potentials and electron affinities, energetic disorder, charge mobility, and eventually current-voltage characteristics can be extracted from simulations.

The paper is organized as follows: In Section 2 we recapitulate the methods required to compute charge transfer rates in (microscopic) morphologies. Section 3 deals with the construction and validation of coarse-grained models. Section 4 discusses how lattice models can be parametrized from an atomistic reference. In Section 5 we review efficient kinetic Monte Carlo algorithms needed to simulate charge transport in systems with large energetic disorder. We then present device simulations and a comparison to experiments in Section 4. Finally, in Section 8 we review computer-simulation-predicted material properties for a number of OLED materials, including BTDF, TBFMI, BCP, Alq3, and  $\alpha$ -NPD.

## 2. Microscopic Modeling

We will begin with the computationally most demanding approach, which is later used as a reference for constructing coarser charge-transport models. For relatively small systems of  $\approx 10^4$  molecules it is possible to parametrize the master equation for charge/exciton transport by combining first-principles and classical force-field-based methods.<sup>[14–17]</sup> First, for every molecule type, the potential energy surface, reorganization energy, ionization potential, and electron affinity, as well as distributed multipoles and polarizabilities are evaluated using first-principles calculations. These are used to parametrize the classical (polarizable) force field and to simulate amorphous morphologies. The polarizable force field is also employed to evaluate the electrostatic and induction interactions of a localized charge with the environment in a perturbative fashion.<sup>[32]</sup> Finally, electronic coupling elements and rates are computed and used to formulate the master equation. The solution of the master equation yields charge carrier mobility and occupation probabilities in the system. This scheme has been applied to study transport in a number of organic semiconducting materials,



thesis was in the field of density functional theory at Peter Grünberg Institute, Forschungszentrum Jülich.

**Pascal Kordt** is a Ph.D. student at the Max Planck Institute for Polymer Research, working on computer simulations of morphology and charge transport in organic semiconductors for OLEDs and photovoltaic cells. His focus is on coarse-grained and stochastic models for large-scale simulations and effects of finite charge density, as well as kinetic Monte Carlo simulations. He studied Physics and in parallel Mathematics at RWTH Aachen University and Queen Mary, University of London. His final year



**Falk May** is a researcher at BASF SE Ludwigshafen, specialized in simulations of OLED materials. His Ph.D. thesis was conducted at the Max Planck Institute for Polymer Research, where he worked on molecular dynamics simulations and the calculation of charge transfer rates with a focus on energy landscapes and reorganization energy in organic semiconductors. He obtained his Physics Diploma from Goethe University of Frankfurt am Main.



phorescent molecules and charge and exciton transport in organic semiconductors.

**Christian Lennartz** is a team leader at BASF SE Ludwigshafen, dealing with modeling of organic electronics at various scales. He is a quantum chemist by training and received his Ph.D. from the University of Bonn, working with ab initio calculations in the field of porous silicon and organic reaction mechanisms. After a postdoctoral stay at BASF SE Ludwigshafen in the field of QM/MM methods for enzyme catalysis he joined BASF SE as permanent staff. His main research interests are photophysics of phos-



tions of complex fluids from the University of Bristol, UK (group of Prof. M. P. Allen). He joined MPIP as a Humboldt Fellow doing theoretical studies of the slippage effect, mechanical properties of polyelectrolyte microcapsules, and effective interactions in colloidal systems.

**Denis Andrienko** is a project leader at the Max Planck Institute for Polymer Research working on the development of multiscale simulation techniques for charge and exciton transport in conjugated polymers as well as small molecular weight organic semiconductors. After completing his Masters degree in the University of Kiev he obtained his first Ph.D. in optics/structural transitions in liquid crystals from the Institute of Physics, Ukraine (group of Prof. Reznikov) and his second Ph.D. on computer simulations of complex fluids from the University of Bristol, UK (group of Prof. M. P. Allen). He joined MPIP as a Humboldt Fellow doing theoretical studies of the slippage effect, mechanical properties of polyelectrolyte microcapsules, and effective interactions in colloidal systems.

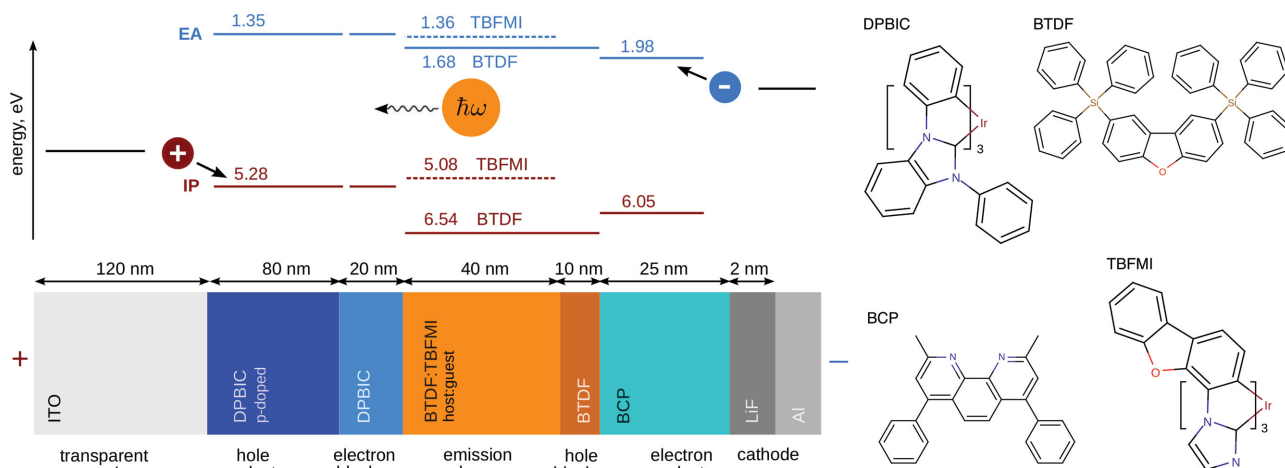


**Figure 1.** Multilayered structure of an OLED with corresponding energy levels and chemical structures. Electrons/holes move upward/downward in energy due to an applied voltage. Higher electron/hole energy levels correspond to smaller electron affinities/ionization potentials. In this OLED, DPBIC (Tris[(3-phenyl-1H-benzimidazol-1-yl-2(3H)-ylidene)-1,2-phenylene]Ir) is used in the hole-conducting layer; TBFMI (Tris[(1,2-dibenzofurane-4-ylene)(3-methyl-1/1-imidazole-1-yl-2(3/1)-ylidene)]Ir(III)) is the emitter (guest); BTDF (2,8-bis(triphenylsilyl)dibenzofurane) is the host material and 2,9-dimethyl-4,7-diphenyl-1,10-phenanthroline (bathocuproine, BCP) is the electron conductor.

such as tris(8-hydroxyquinoline) aluminum (Alq3),<sup>[17,33–35]</sup> fullerene (C60) and its derivatives,<sup>[36,37]</sup> dicyanovinyl-substituted oligothiophenes,<sup>[18,19,38]</sup> poly(3-hexylthiophene) (P3HT),<sup>[22]</sup> and poly(bithiophene-alt-thienothiophene) (PBTTT),<sup>[23]</sup> to name a few.

In the next sections we briefly recapitulate the methods used to evaluate the ingredients of charge transfer rates. These will later be used to parametrize coarse-grained models of an organic semiconductor.

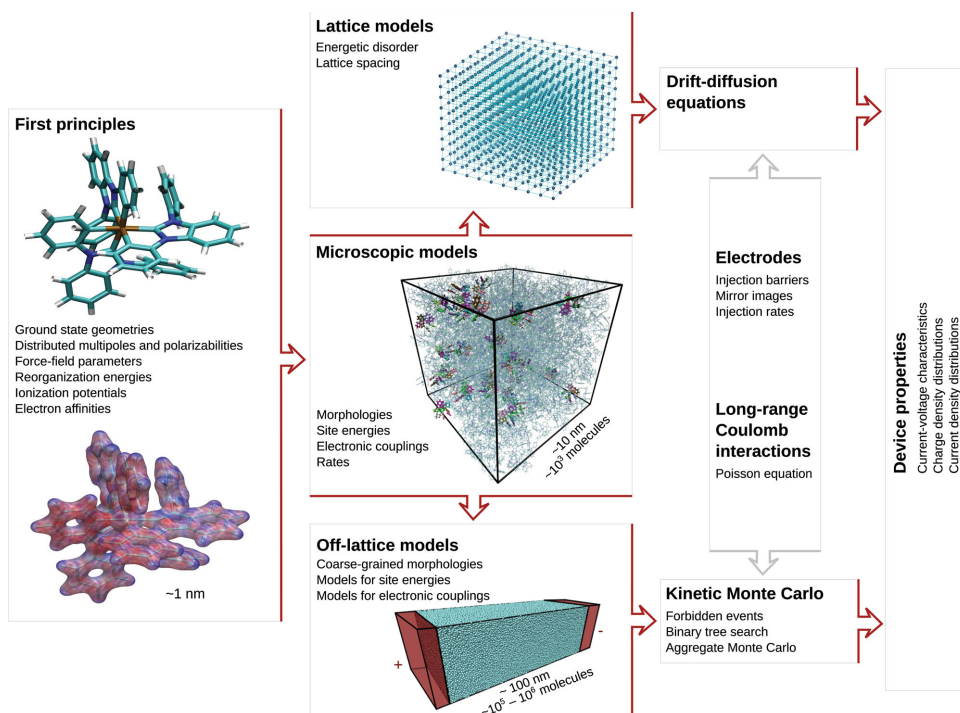


**Figure 2.** Possible workflows of parameter-free OLED simulations: polarizable force-fields and electronic properties of isolated molecules obtained from first principles are used to generate amorphous morphologies and evaluate charge transfer rates in small systems (microscopic models). Coarse-grained models are parametrized either by matching macroscopic observables, e.g., charge mobility, of the microscopic and coarse-grained (lattice) models. The resulting analytical expressions for mobility are then used to solve drift-diffusion equations for the entire device, after incorporating long-range electrostatic effects and electrodes. Alternatively, off-lattice models can be developed by matching distributions and correlations of site energies, electronic couplings, and positions of molecules. The master equations for this model can be solved using the kinetic Monte Carlo algorithm, yielding macroscopic characteristics of a device.

## 2.1. Morphology

In general, predicting realistic molecular arrangements of organic semiconductors is a challenging task: organic materials can be highly crystalline, form partially ordered liquid crystalline, smectic, or lamellar mesophases, or be completely amorphous. Many are polymorphs and practically all have a fairly high density of defects, which has a large impact on their conductive properties.<sup>[18,19]</sup> X-ray scattering, tunneling electron microscopy (TEM), and solid-state nuclear magnetic resonance (NMR) spectroscopy are common experimental techniques which are used to probe molecular ordering of organic materials.<sup>[39–41]</sup> Organic semiconductors employed in OLEDs are usually amorphous, which simplifies modeling of their morphologies.

In order to simulate large-scale morphologies, atomistic and coarse-grained models are often employed. Both rely on force fields, i.e., parametrizations of the potential energy surface of intermolecular (nonbonded) and intramolecular (bonded) interactions. While for biomolecules a number of force fields exist and can be used “out of the box,” this is normally not the case for organic semiconductors, which have extended  $\pi$ -conjugated systems. Such compounds require—at least partial—reparametrizations of existing force fields. For bonded interactions this can be performed by scanning the cross-sections of the potential energy surface (e.g., dihedral potentials) using first-principles methods,<sup>[34,42,43]</sup> as illustrated for DPBIC in **Figure 3**, where two potential energy surfaces are shown, one of the bending of a benzene ring out of the ligand plane ( $\gamma$ ) and the other one of its rotation out of this plane ( $\beta$ ).

The situation with nonbonded interactions is more complex: Coulomb and Lennard-Jones potentials can also be parametrized by using first-principles calculations.<sup>[32]</sup> This, however, requires distributed multipoles and polarizabilities, as well as many-body van der Waals interactions, making force-evaluation computationally demanding. As a compromise, most force fields account for the induction contribution by adjusting partial charges and van der Waals parameters. These parametrizations are, however, state-point dependent and should be validated against experimental data.

With the force field at hand, an amorphous morphology of an OLED layer can be simulated by using Monte Carlo or molecular dynamics (MD) techniques.<sup>[14,17,44,45]</sup> Several

protocols were suggested for this purpose. One can, for example, anneal the system above the glass transition temperature, and then quench to room temperature using the *NPT* ensemble.<sup>[19]</sup> It is also possible to use Monte Carlo<sup>[33,44]</sup> or molecular dynamics simulations to gradually deposit the material.<sup>[46]</sup> Due to large deposition rates in molecular dynamics, simulated morphologies can be very far from equilibrium, while the Monte Carlo technique does not control the kinetics of the deposition process.

As an illustration, an amorphous morphology of DPBIC, simulated using the annealing protocol, is shown in **Figure 2**. Here, the Berendsen barostat and thermostat<sup>[47]</sup> were used and the system was first equilibrated at 700 K for 1 ns, then quenched to 300 K and equilibrated for another 1.3 ns. The final density of the system was 1.29 g cm<sup>-3</sup>, which corresponds to a number density of 8.50 × 10<sup>20</sup> cm<sup>-3</sup>.

## 2.2. Charge Transfer

Charge transport in organic materials is intimately linked to the underlying material morphology: in crystals and at low temperatures transport is coherent, charges are delocalized, and consequently a bandlike transport prevails.<sup>[48–50]</sup> At higher temperatures intramolecular and intermolecular vibrations destroy the coherence, charges become localized by the dynamic disorder and transport becomes diffusive.<sup>[51–54]</sup> In disordered materials with weak electronic couplings between molecules, static disorder localizes charged states already at low temperatures and a thermally-activated hopping transport dominates.<sup>[55]</sup> Descriptions of transport in polymeric systems are the most challenging: along chains it can be diffusion-limited by dynamic disorder while between the chains it is in the hopping limit.<sup>[56,57]</sup>

Since we are dealing with amorphous materials, we assume thermally-activated type of transport (this can be verified experimentally by studying temperature- and field-dependencies of mobility). The simplest expression for a charge transfer rate which takes into account energetic landscape, polaronic effects, and electronic coupling elements, is the semi-classical Marcus rate<sup>[58,59]</sup>

$$\omega_{ij} = \frac{2\pi}{\hbar} \frac{J_{ij}^2}{\sqrt{4\pi\lambda_{ij}k_B T}} \exp\left[-\frac{(\Delta E_{ij} - \lambda_{ij})^2}{4\lambda_{ij}k_B T}\right] \quad (1)$$

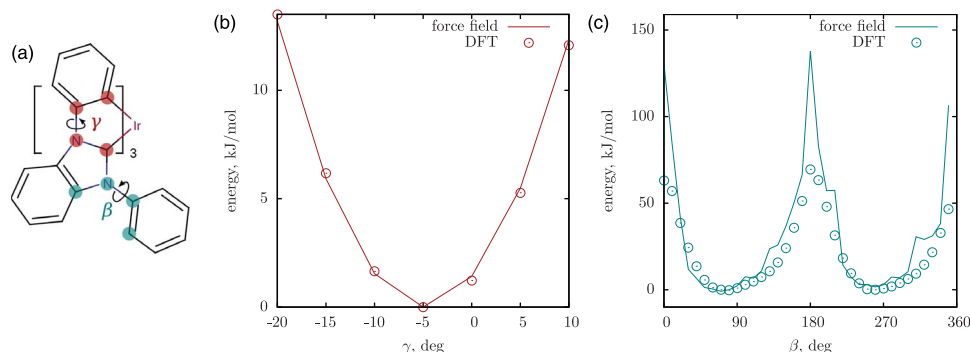


**Figure 3.** Examples of the potential energy scans of the dihedral angles  $\gamma$  (b) and  $\beta$  (c), shown in a). DFT calculations (B3LYP/6–311g(d,p)) and the force field cross sections (after adjusting its parameters) of the potential energy surfaces are shown in b,c).

Here the reorganization energy,  $\lambda_{ij}$ , reflects the effect of molecular rearrangement in response to the change of the charge state, the electronic coupling element,  $J_{ij}$ , describes the strength of the electronic coupling between two localized (diabatic) states, and  $E_{ij} = E_i - E_j$  is the driving force, where  $E_i$  is the site energy of molecule  $i$ .<sup>[60]</sup>

Note that the semiclassical Marcus rate is the high temperature limit of a more general, quantum-classical rate<sup>[61]</sup> and as such has a limited range of applicability. There exist also other rate expressions, which go beyond the harmonic approximation for the thermal bath<sup>[62–64]</sup> and have been reported to describe experimental data in a wide temperature and field range.<sup>[65]</sup>

The distribution of rates for DPBIC, evaluated using the semi-classical rate expression, Equation (1), is shown in Figure 5e. This distribution is very broad, with rates varying by several orders of magnitude, which is typical for amorphous systems. Large variations are a result of pronounced energetic disorder (see Section 2.3), as well as of a broad distribution of electronic couplings (see Section 2.5).

### 2.3. Site Energies

Site energy differences, or driving forces, which enter the charge transfer reaction rate, Equation (1), can be evaluated perturbatively: first the ionization potential (IP, hole transfer) or electron affinity (EA, electron transfer) of an isolated molecule is calculated and then the interaction with the environment (electrostatic and polarization) is accounted for

$$E_i = E_i^{\text{int}} + E_i^{\text{el}} + E_i^{\text{pol}} + q\mathbf{F} \cdot \mathbf{r}_i \quad (2)$$

Here  $\mathbf{F}$  is the external electric field,  $\mathbf{r}_i$  is the center of mass of a molecule, and  $q$  is its charge. The IP and EA can be evaluated using first principles methods as the energy difference of a charged molecule (in its charged geometry) and a neutral molecule (in its neutral geometry), i.e.,  $E^{\text{int}} = U_{\text{c}} - U_{\text{n}}$ , where the first (lowercase) index denotes the charge state and the second (uppercase) index denotes the geometry.

The interaction with the environment is often computed on a classical level, using distributed multipoles<sup>[66]</sup> and polarizabilities.<sup>[67–69]</sup> For each molecule  $i$  the electrostatic interaction,  $E_i^{\text{el}}$ , is evaluated for all molecules in a sphere of a certain radius (cutoff). Note that, even in amorphous materials, an ample cutoff is required to converge the electrostatic energy. For molecular assemblies with a long-range orientational or positional order it is often not feasible to achieve the convergence by increasing the cutoff radius<sup>[70]</sup> and the long-range Coulomb interaction energy should be evaluated using the Ewald summation technique.<sup>[69–72]</sup>

The induction interaction energy,  $E_i^{\text{pol}}$ , can be evaluated using the Thole model.<sup>[67,68]</sup> For organic molecules the Thole parameters must be adjusted to reproduce the molecular polarizability tensor. Normally, the induction contribution converges for much smaller cutoffs than the electrostatic one, though special care should be taken in order not to have artificially induced dipoles at the surface of the cutoff sphere (e.g., by choosing a larger electrostatic cutoff radius than the polarization one).

In order to evaluate site energies (their differences drive charge transfer reactions) for an amorphous morphology of

DPBIC, we have used an adapted version of the Ewald summation method for long-range electrostatic interactions<sup>[67,69–72]</sup> (i.e., the electrostatic contribution is calculated without a cutoff) and the Thole model with a cutoff of 3 nm for the induction interaction. Atomic charges, fitted to reproduce the molecular electrostatic potential (shown in Figure 2), were used for electrostatic calculations, while Thole parameters were adjusted to reproduce the molecular polarizability tensor of DPBIC. The energetic landscape, shown in Figure 4b, is spatially correlated, which is due to a long-range dipolar electrostatic contribution.<sup>[26,73]</sup> This can be seen qualitatively in the cross-section of the potential energy landscape, Figure 4b, and quantified by the autocorrelation function,  $\kappa(r)$ , shown in Figure 4c. The distribution of site energies is approximately Gaussian with a width of  $\sigma = 0.176$  eV. Note that the Gaussian shape of the distribution is only expected if the change in the molecular polarizability upon charging is small,<sup>[21]</sup> which is indeed the case for DPBIC: one third of the trace of the polarizability tensor is 108.5 Å<sup>3</sup> for a neutral molecule and 127.1 Å<sup>3</sup> for a cation (B3LYP/TZVP).

### 2.4. Reorganization Energy

The reorganization energy,  $\lambda_{ij}$ , quantifies the energetic response of a molecule due to its geometric rearrangement upon charging or discharging. It has two contributions: the internal (intramolecular) part, i.e., the energy difference due to the internal molecular degrees of freedom, and the outersphere (intermolecular) part, which is due to the relaxation of the environment.<sup>[60]</sup> The internal part is normally evaluated as the energy difference of the involved charged/neutral states in a charged/neutral geometry using density functional calculations in vacuum.<sup>[74]</sup> The outersphere contribution can be computed using the dielectric response function,<sup>[17]</sup> polarizable force fields,<sup>[75]</sup> or hybrid quantum mechanics/molecular mechanics methods.<sup>[76]</sup>

For DPBIC the calculated (B3LYP, 6–311g(d,p)) internal reorganization energies for hole transport are 0.068 eV (discharging) and 0.067 eV (charging). Here we neglect the outersphere contribution, which becomes important in strongly polarizable environments.

### 2.5. Electronic Couplings

Evaluation of electronic coupling elements,  $J_{ij}$ , between the initial and the final states of a charge transfer complex (molecular dimer) requires the knowledge of diabatic states and the Hamiltonian of a dimer. Diabatic states are often approximated by the highest occupied molecular orbital (HOMO) of monomers in case of hole transport and the lowest unoccupied molecular orbital (LUMO) for electron transport<sup>[77–79]</sup> (“frozen core” approximation) or constructed using the constrained density functional approach.<sup>[80]</sup> In some cases the explicit evaluation of the dimer Hamiltonian can be avoided by employing semiempirical methods.<sup>[74,81–83]</sup>

Electronic couplings are intimately connected to the overlap of electronic orbitals participating in a charge transfer reaction and are therefore very sensitive to relative molecular positions and orientations. Together with the energetic landscape, they

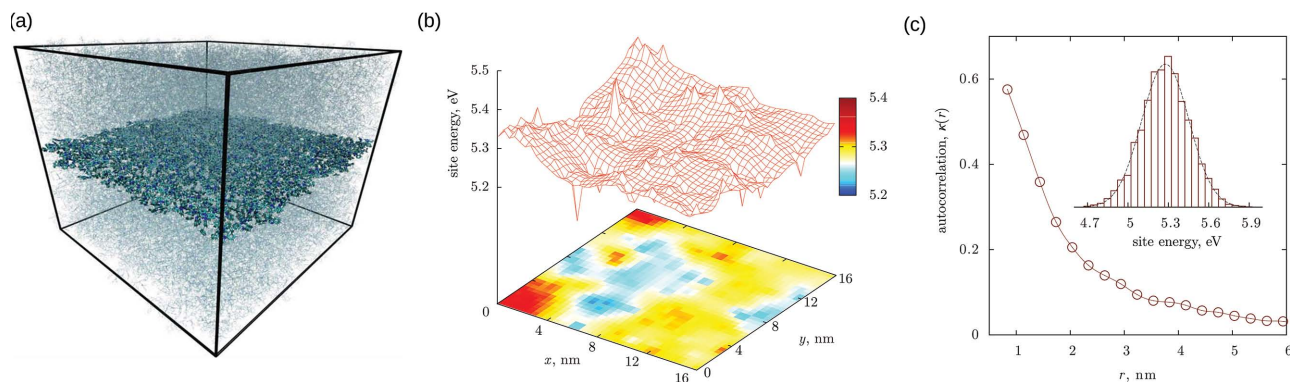


**Figure 4.** a) Amorphous morphology of DPBIC with a highlighted one-molecular-layer thick cross-section for which the energetic landscape is shown in b). c) The spatial autocorrelation function of site energies,  $\kappa(r)$ . Inset: The distribution of site energies, which is approximately Gaussian with a mean of 5.28 eV and energetic disorder of 0.176 eV.

constitute one of the main factors which influence charge transport in organic semiconductors.<sup>[18,19,84,85]</sup> Depending on the first-principles method and approximations used, computed electronic coupling elements can easily vary by a factor of ten.<sup>[86,87]</sup>

For the amorphous morphology of DPBIC, the distribution of electronic couplings of molecular pairs at a certain distance is approximately Gaussian with a mean decaying exponentially for intermolecular separations larger than 1.1 nm, see Figure 5d. Below this distance electronic couplings are constant (on average) and are of the order of  $10^{-3}$ – $10^{-2}$  eV. Such a behavior has also been observed for amorphous mesophases of Alq3 and DCV4T.<sup>[29,30]</sup>

### 3. Coarse-Grained Models

The microscopic model outlined in Section 2, in combination with the charge dynamics simulations (see Section 5), provides a direct link between the molecular structure and macroscopic observables, e.g., charge mobility. It is, however, limited to relatively small systems of  $\approx 10^4$  molecules, which is far from sizes required for studying, e.g., rare events during material degradation. Furthermore, one can have pronounced finite size effects, especially in materials with large energetic disorder.<sup>[29,35]</sup>

In view of this, various coarse-grained models have been developed.<sup>[29,88,89]</sup> The idea behind these models is to reproduce the key morphological and electronic properties of the underlying materials without explicit simulations of atomistic morphologies, evaluations of electronic couplings and site energies. The link to the chemical composition is retained by an appropriate parametrization of mesoscopic-scale quantities, e.g., distributions and correlations of site energies, electronic couplings, and pair distribution functions of molecular positions, evaluated as described in Section 2. Coarse-grained models allow studying charge dynamics in systems of more than  $10^6$  molecules. In what follows we describe how such models can be parametrized.

#### 3.1. Morphology

The first step in constructing a coarse-grained model is the prediction of molecular positions. In the general case, the

algorithm should reproduce all (including many-body) correlation functions of molecular positions in the reference morphology. For amorphous molecular arrangements, however, the pair distribution function is sufficient to adequately describe the molecular ordering. Thus, one has to develop an algorithm that generates point positions of a specified density and reproduces the radial distribution function,  $g(r)$ , of the microscopic model.

To do this, one can use a Poisson process.<sup>[29,30]</sup> This process first positions  $N$  uniformly distributed points in a volume  $w$ ,  $N \sim \text{Poi}(\rho w)$ , where  $\rho$  is the point density. Unphysically close contacts are removed by assigning a random radius  $R_n$  to every point  $n$  and by deleting the points whose sphere is contained in the sphere of another point  $m$ . The point density is then adjusted by introducing more points in the voids. This procedure is repeated iteratively until the desired density,  $\rho$ , is reached. The algorithm yields reasonably good approximations of  $g(r)$ .<sup>[29,30]</sup>

An exact match of the radial distribution function can be achieved by using techniques employed in soft condensed matter simulations, namely, the iterative Boltzmann inversion (IBI)<sup>[90,91]</sup> or inverse Monte Carlo<sup>[92–94]</sup> methods. Both rely on the Henderson theorem,<sup>[95]</sup> which states that for every  $g(r)$  there is a unique (up to an additive constant) interaction potential,  $U(r)$ , such that sampling the system in the canonical ensemble reproduces this  $g(r)$ . Hence, it suffices to construct an algorithm capable of finding  $U(r)$  from a given  $g(r)$ . In IBI, this is done by simulating a coarse-grained system with a potential which is iteratively refined at the  $i$ th iteration as

$$U^{i+1}(r) = U^i(r) - k_B T \ln \left[ \frac{g^i(r)}{g^{\text{ref}}(r)} \right] \quad (3)$$

A potential that reproduces the reference radial distribution function is a fixed point of this relation. In practice, the second term is rescaled by a factor between 0 and 1 to make the algorithm numerically stable. Inverse Monte Carlo follows the same idea, except that the correction to the potential is rigorously derived (in a linear approximation) and contains cross-correlations of the number of particles at different separations  $r$ .<sup>[92–94]</sup> Both methods are implemented in the VOTCA software package.<sup>[96]</sup>

Figure 5 a shows the radial distribution functions of a small atomistic (reference) systems of 4000 DPBIC molecules and of

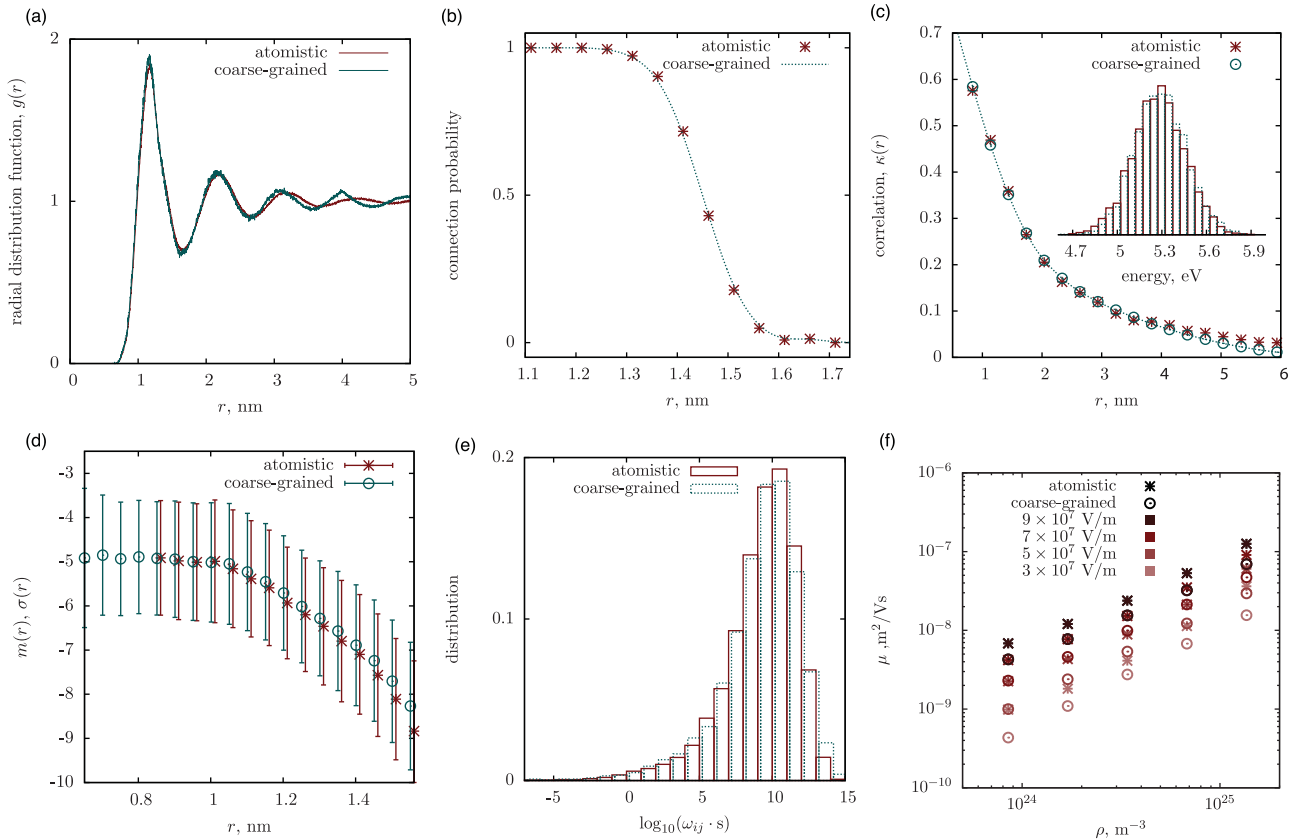


**Figure 5.** Comparison of the atomistic ( $17 \times 17 \times 17 \text{ nm}^3$ ) and coarse-grained ( $50 \times 50 \times 120 \text{ nm}^3$ ) models. a) Radial distribution function,  $g(r)$ . b) Probability of two sites to be connected (added to the neighbor list) as a function of their separation. c) Spatial site energy autocorrelation function,  $\kappa(r)$ ; Inset: Site energy distribution. d) Mean  $m$  and width  $\sigma$  of a distribution of the logarithm of electronic couplings,  $\log_{10}(J^2/eV^2)$ , for molecules at a fixed separation  $r$ . e) Rate distributions. f) Mobility as a function of hole density, plotted for four different electric fields.

a much larger system of 255 083 interacting points generated using the potential inverted with the IBI procedure. Note that the generation of the coarse-grained morphology is very fast, since there are significantly less degrees of freedom involved as well as the smooth coarse-grained interaction potential leads to much faster (molecular) dynamics and hence shorter equilibration times. In total, 250 000 steps (1 ns) were used to equilibrate the system of 255 083 interacting points in the *NPT* ensemble, starting from a lattice.

### 3.2. Site Energies

Early models for charge transport simulations assumed a Gaussian distribution of width  $\sigma$  of spatially uncorrelated<sup>[25]</sup> or correlated<sup>[26]</sup> site energies, where  $\sigma$  is referred to as the energetic disorder of the system. In the spatially correlated model, all molecules are assumed to have randomly oriented dipole moments,  $\mathbf{p}$ , of fixed magnitude. The site energies,  $E_i$ , are then evaluated as

$$E_i = -\sum_{j \neq i} \frac{q\mathbf{p}_j \cdot (\mathbf{r}_j - \mathbf{r}_i)}{\epsilon |\mathbf{r}_j - \mathbf{r}_i|^3} \quad (4)$$

where  $q$  is the charge,  $\mathbf{r}_i$  is the position of molecule  $i$  and  $\epsilon$  is the material's relative permittivity. This sum, evaluated using the Ewald summation method,<sup>[71]</sup> has a spatial correlation function  $\kappa(r) \equiv \langle \text{corr}[E_i, E_j] \rangle$  which decays approximately as  $1/r$ , where the average is taken over all molecules with center-of-mass distance  $|\mathbf{r}_j - \mathbf{r}_i| = r$ .

Since the spatial correlation function can deviate from the  $1/r$  asymptotics<sup>[29]</sup> (e.g., when the molecular dipole also varies,<sup>[19,29]</sup> an algorithm that can reproduce any (physically relevant) spatial correlation function is required. For Gaussian-distributed site energies this can be achieved by mixing in the energy values of the neighbors: for each site  $A$ ,  $N$  independent Gaussian distributed random variables  $X_i^A \sim \mathcal{N}(0,1)$ ,  $0 \leq i \leq N$ , are drawn. The energy of the molecule is then calculated as

$$E^A = \sqrt{a}X_0^A + \sum_{i=1}^N \sqrt{\frac{b_i}{\ell_i^A}} \sum_{B \in S(r_i, A)} X_i^B \quad (5)$$

where  $S(r_i, A)$  denotes a sphere of radius  $r_i$  around molecule  $A$  and  $\ell_i^A$  is the number of molecules within this sphere. The first term in Equation (5) corresponds to an uncorrelated energetic landscape. By adjusting  $a$ , one can change the energetic disorder,  $\sigma$ , without affecting the spatial correlation function  $\kappa(r)$ .

The sum over molecules within a certain cutoff  $r_i$  adds spatial correlations. By adjusting the weighting coefficients,  $b_i$ , one can reproduce the reference correlation function. It is also possible to devise an iterative scheme which converges to a set of required weights.

For DPBIC, the autocorrelation functions of the reference (evaluated in the atomistic system) and the coarse-grained (constructed by iteratively refining the weighting coefficients) systems are shown in Figure 5c. The autocorrelation function is perfectly reproduced and, in fact, is far from the  $1/r$  dependence assumed in lattice models.

### 3.3. Neighbor List

Since electronic coupling elements decrease exponentially with intermolecular separation, charge transfer reactions normally happen only between nearest molecular neighbors. This physical argument is frequently used to reduce the size of the list of molecular pairs (neighbor list) for which charge transfer rates are evaluated. In atomistic simulations the neighbor list is constructed based on the cutoff for the shortest distance between  $\pi$ -conjugated molecular fragments.<sup>[17]</sup> In a coarse-grained model, where the molecular information is not available, the neighbor list can be constructed by analyzing the probability in the reference system of two molecules at a certain separation to be connected. This distribution is shown in Figure 5b. One can see that all molecules separated by less than a certain minimal distance,  $r_{\min}$ , are connected while there are no connected pairs if separation exceeds  $r_{\max}$ . In the coarse-grained model each pair of sites is then connected based on this probability distribution.

For DPBIC, this approach reproduces well both the connectivity of the reference system (see Figure 5b)) and the coordination number (11.60 for the atomistic and 11.44 for the coarse-grained model).

### 3.4. Electronic Couplings

To treat electronic coupling elements, one can analyze the distance-dependent distribution  $P[J_{ij}(r)]$ , i.e., the distribution of electronic couplings at a given separation  $r$ . For amorphous systems it has been found that the logarithm of the coupling element,  $\log(J_{ij}^2(r)/eV^2)$ , is Gaussian distributed with a mean  $m(r)$  and standard deviation  $\sigma(r)$  which depend on the molecular separation.<sup>[29,30]</sup> The exponential decay of  $J_{ij}(r)$  with intermolecular separation results in a linear decrease of the mean of the distribution for  $r \geq 1.1$  nm, as shown in Figure 5d. To reproduce this behavior in a coarse-grained model, the values for the logarithm of the coupling are drawn from the normal distribution,  $\log(J_{ij}(r)^2/eV^2) \sim \mathcal{N}(m(r), \sigma^2(r))$ , where  $m(r)$  and  $\sigma(r)$  are chosen according to the atomistic reference.

### 3.5. Charge Mobility and Model Validation

The coarse-grained model can be validated by comparing the charge transfer rates, as well as the mobility–field and mobility–charge density dependencies of both models. The rate

distributions are shown in Figure 5e and are in good agreement with each other. The mobility versus charge density is shown in Figure 5f for different electric fields and also agrees with each other, validating the coarse-grained model. Small deviations are due to statistical fluctuations in relatively small systems studied (4000 molecules).

## 4. Lattice Models

In Section 3 we have described how to parameterize a coarse-grained model based on a microscopic reference and use it to simulate relatively large (mesoscopic) systems. Alternatively, one can adopt an approach often employed to analyze experimental data, where analytical expressions for charge mobility are parametrized by fitting the *IV* characteristics of, e.g., a simple diode. The expressions themselves are derived with the help of lattice-based models, such as the Gaussian disorder model,<sup>[25]</sup> the extended Gaussian disorder model (EGDM), which includes the effect of electron density,<sup>[27]</sup> the correlated Gaussian disorder model (CDM), which takes into account spatial correlations of site energies,<sup>[26]</sup> or the extended correlated Gaussian disorder model (EGDM).<sup>[28]</sup>

In principle, some parameters of these models can be obtained by analyzing the microscopic model directly: the energetic disorder,  $\sigma$ , for example, can be calculated from the site energy distribution, as described in Section 2.3. The lattice constant,  $a$ , can be estimated by matching the densities of the atomistic and lattice models, i.e.,  $a = (V/N)^{1/3}$ , where  $V$  is the volume and  $N$  is the number of molecules. In practice, however, it is better to obtain the model parameters by fitting the mobility to results of atomistic or stochastic simulations. The reason for this is that the analytical expressions provided by the lattice models rely on certain approximations, which might not hold for the microscopic model. For example, spatial correlations of site energies, present in the microscopic model, can be accounted for the smaller energetic disorder in the GDM model. By comparing the two approaches one can then assess whether or not a particular lattice model is capable of reproducing material properties<sup>[29]</sup> or can be used in drift-diffusion simulations of devices.<sup>[97]</sup>

As an example, a mobility versus charge density fit has been performed for an amorphous DPBIC morphology. To correct for finite-size effects at small charge densities, an extrapolation procedure was used to obtain nondispersive mobilities<sup>[35]</sup> via a simulation of charge transport at high temperatures and a subsequent extraction of the room-temperature mobility from the known mobility-temperature dependence, as shown in Figure 6a. The extrapolated values, together with mobilities at charge densities typical for an operating OLED, were used to fit the EGDM and ECDM models, as shown in Figure 6b. Notably, the model with energetic correlations yields a worse fit than the uncorrelated one, even though spatial site energy correlations are present in the system. This has been observed before in simulations of amorphous dicyanovinyl-substituted quaterthiophene.<sup>[29]</sup> The reason is that the spatial correlation function of site energies does not decay as  $1/r$  at large  $r$ , as correlated disorder models predict. This is also reflected in the fitting parameters, which are summarized in Table 1: for

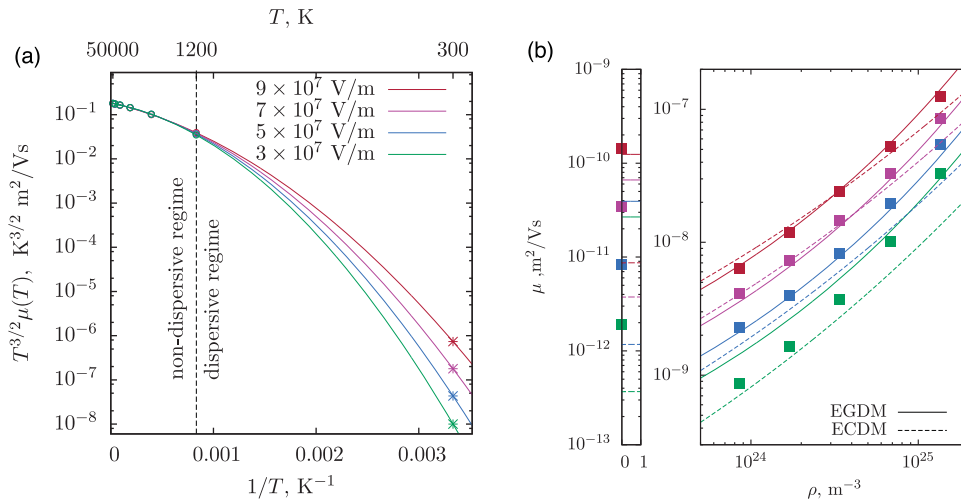


**Figure 6.** a) Extrapolation of high-temperature mobility simulations to room temperatures. For a system of 4000 molecules transport simulations with one carrier are nondispersive only above 1200 K. Hence, mobilities in the temperature range between 1200 and 50 000 K (circles) are used for extrapolations to nondispersive mobility values at 300 K (crosses). b) A fit to EGDM (solid lines) and ECDM (dashed lines) models. All four dependencies are fitted simultaneously.

both EGDM and ECDM models the estimated energetic disorder differs from the microscopic value by about 0.04 eV. The EGDM underestimates the disorder, while the ECDM overestimates it. Similarly, the microscopic zero-field mobility,  $\mu_0$ , is in between the two fitted values. The absence of correlations in the EGDM is compensated by an effectively increased lattice constant, while in the ECDM the lattice constant is much smaller than the density-based estimate. Note that both models were originally developed for energetic disorder up to 0.15 eV, while here the atomistic and ECDM values are higher than this.

## 5. Charge Dynamics

The outcome of both, coarse-grained and atomistic, models are center-of-mass positions of molecules and charge transfer rates between them, i.e., a directed graph. To model charge dynamics in this network, one needs to solve the corresponding master equation. While the efficiency of the solver is not important for relatively small systems, it becomes essential for modeling transport in large coarse-grained systems of millions of sites. Here we summarize several approaches which help to make these solvers computationally efficient.

### 5.1. Master Equation

Our target is the solution of the master equation, which describes the time evolution of the system

$$\frac{dP_i(t)}{dt} = \sum_j [T_{ij}P_j(t) - T_{ji}P_i(t)] \quad (6)$$

where  $P_i$  is the (unknown) probability of state  $i$  and  $T_{ij}$  is the transition probability from state  $i$  to  $j$ . For one charge carrier, the state of the system is given by the index of the charged

molecule and the rates are equal to charge transfer rates, i.e.,  $P_i = p_i$ , where  $p_i$  is the occupation probability of a site  $i$ , and  $T_{ij} = \omega_{ij}$ .

This equation can be solved analytically in some special cases. In general, however, direct numerical differential equation solvers are used.<sup>[98]</sup> If more than one charge carrier is present in the system, the number of system states increases rapidly (it is proportional to the binomial coefficient) and ordinary differential equation (ODE) solvers quickly become impractical unless additional approximations are employed. One of them is the mean-field approximation, which allows to rewrite the master Equation (6) in terms of site-occupation probabilities,  $p_i$ ,

$$\frac{dp_i}{dt} = \sum_j [\omega_{ij}p_j(1-p_i) - \omega_{ji}p_i(1-p_j)] \quad (7)$$

One can see that the differential equation becomes nonlinear, with the  $1-p$  term accounting for the prohibited double occupancy of a site in a mean-field way.

An alternative approach to solve the master equation is to use kinetic Monte Carlo (KMC) algorithms,<sup>[99,100]</sup> i.e., to construct a continuous-time Markov process, where the probability of a certain event to occur depends only on its current state. We will discuss particular implementations of KMC in the next sections.

**Table 1.** Lattice spacing,  $a$ , energetic disorder,  $\sigma$ , and mobility at zero field and in the limit of zero charge density for the microscopic, EGDM, and ECDM models. The last row corresponds to the experimentally measured  $IV$ -characteristics fitted to the ECDM model.

	$a$ [nm]	$\sigma$ [eV]	$\mu_0$ (300 K) [ $\text{m}^2 \text{V}^{-1} \text{s}$ ]
Microscopic	1.06	0.176	$3.4 \times 10^{-12}$
EGDM, simulation	1.67	0.134	$2.1 \times 10^{-11}$
ECDM, simulation	0.44	0.211	$1.8 \times 10^{-13}$
ECDM, experiment	0.74	0.121	$1.2 \times 10^{-10}$

Since KMC does not rely on the mean-field approximation, it is possible to evaluate the error introduced by neglecting higher-order correlations. It turns out that for an energetic disorder of  $\sigma/k_B T = 2$  the correction due to pair correlations is smaller than 3%.<sup>[101]</sup> In more disordered systems this error increases, as well as it is not clear how higher order correlations might affect this result.

Once the equation for  $p_i$  is solved, the mobility tensor,  $\mu$ , can be evaluated as

$$\mu_{\alpha\beta} = \frac{1}{\rho F^2 V} \sum_{ij} \omega_{ij} p_i (1 - p_j) r_{ij,\alpha} F_\beta \quad (8)$$

where  $\rho$  is the charge density,  $F$  is the external electric field,  $V$  is the box volume, and  $r_{ij} = |\mathbf{r}_i - \mathbf{r}_j|$ . It is also possible to compute the mobility tensor from the KMC trajectory

$$\mu_{\alpha\beta} = \frac{1}{N} \sum_{i=1}^N \frac{\langle v_{i,\alpha} F_\beta \rangle}{F^2} \quad (9)$$

where  $\langle \mathbf{v}_i \rangle$  is the velocity of the  $i$ th carrier,  $\langle \dots \rangle$  denotes the average over the simulation time, and the sum is performed over  $N$  carriers. The mobility at zero external field can also be calculated from the diffusion tensor using the generalized Einstein relation<sup>[102]</sup> (generalization is required due to the Fermi-Dirac and not Boltzmann statistics of the site-occupation probability)

$$qD \frac{\partial \rho}{\partial \eta} = \mu \rho \quad (10)$$

Here  $D_{\alpha\beta} = \langle \Delta r_\alpha \Delta r_\beta \rangle / 2\tau$ , where  $\tau$  is the total simulated time,  $\rho$  is the charge density, and  $\eta$  is the chemical potential. Note that the Einstein relation holds only for a steady state that fulfills the detailed balance condition<sup>[103]</sup> and for small fields;<sup>[104]</sup> it cannot be applied to inhomogeneous temperature distributions<sup>[105,106]</sup> or unrelaxed (“hot”) carriers.

## 5.2. Kinetic Monte Carlo

The variable step size method (VSSM)<sup>[107,108]</sup> is one of the kinetic Monte Carlo solvers of the master equation. It is a hierarchical method, i.e., events can be grouped and VSSM can be used for both the groups and events in the group. In case of charge transport, for example, it is convenient to have two levels: first a charge is selected based on the escape rate,  $\omega_i = \sum_j \omega_{ij}$ , and then the hopping destination is chosen. VSSM allows an efficient treatment of forbidden events,<sup>[108]</sup> without the need to recalculate escape rates at every step. In charge-transport simulations, forbidden events are due to the site single-occupancy constraint which leads to Fermi-Dirac statistics for the equilibrium distribution of site occupations, as shown in **Figure 7a** for a DPBIC morphology of 4000 molecules. As expected, both the Fermi level and occupation probability increase with the increase of charge density. This is explained in **Figure 7b**, where the Gaussian density of states is filled up to the Fermi energy, and the product of the Fermi-Dirac distribution and Gaussian density of states, integrated up to the Fermi energy, gives the charge density in the system.

Note that the standard implementation of the VSSM algorithm would require about  $10^8$  KMC steps to reach the steady state for charge flux in DPBIC, since carriers can be trapped in aggregates of low-energy sites. This can be circumvented using an aggregate Monte Carlo (AMC) algorithm,<sup>[88]</sup> i.e., by coarsening the state space<sup>[109–113]</sup> into “superstates.” Efficient coarsening methods that retain physically sensible trajectories are the stochastic watershed algorithm,<sup>[109,114,115]</sup> which is an improved version of the watershed algorithm,<sup>[116,117]</sup> and a graph-theoretic decomposition.<sup>[118]</sup> AMC has been tested on the amorphous phase of Alq3, where it leads to about two orders of magnitude faster convergence.<sup>[88]</sup>

KMC solvers with explicit long-range Coulomb interactions require rate updates at (practically) every KMC step. Efficiency of such algorithms can be improved by using a binary tree

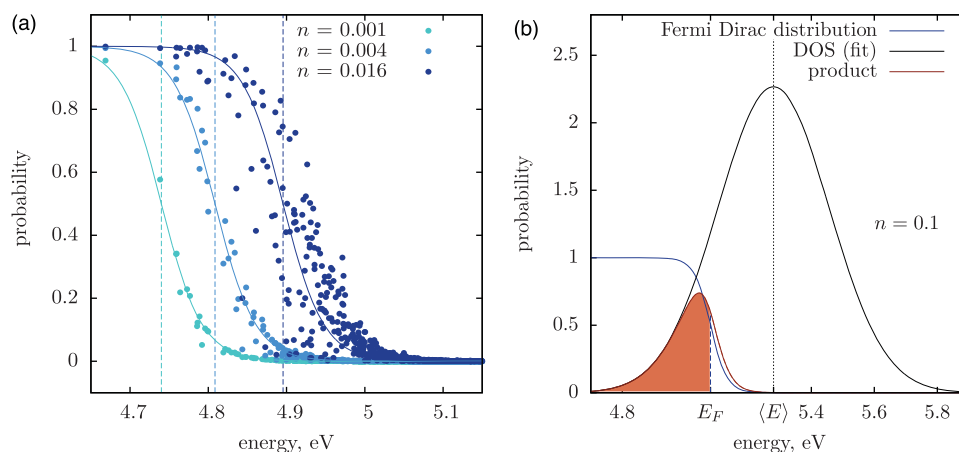


**Figure 7.** a) Site-occupation probability as a function of site energy plotted for three charge densities. Points are Monte Carlo simulations in a DPBIC morphology of 4000 molecules. Solid lines are fits to the Fermi-Dirac distribution. The Fermi level (dashed lines) increases with increasing relative charge density  $n$  (charges per site). b) Filling of the Gaussian density of states (DOS) for a number density of  $n = 0.1$ . The product of the Fermi-Dirac distribution and the Gaussian DOS yields the occupation distribution (red curve). The area under this curve, evaluated up to the Fermi level, is equal to the charge density. The width of the DOS matches the energetic disorder of DPBIC (0.176 eV) and is centered at 5.28 eV.

search and update algorithm.<sup>[119]</sup> It updates only those rates which are affected by a moving carrier and has a logarithmic scaling with the number of events, whereas a linear search scales linearly. The binary tree algorithm becomes more and more beneficial with increasing number of charge carriers: while for 1% carrier density (in 4000 molecules) it is slower than a primitive search, at 10% it is already faster by about a factor of 10.

## 6. Device Simulations

In order to simulate *IV* characteristics of an entire device, two additional ingredients must be incorporated in the model: the effect of metallic electrodes, which inject and collect charges, and the strongly inhomogeneous distribution of charge density in the device. This can be done on a macroscopic level, by complementing the drift-diffusion equations with boundary conditions and Gauss's law for charge density, as described in Section 6.1. An alternative approach is to extend the Monte Carlo scheme by including the electrodes and the Poisson equation solver for long-range electrostatics. This extension has already been implemented for lattices,<sup>[97]</sup> see also Section 6.2, and is discussed for off-lattice models Section 6.3. To disentangle the contributions of different functional layers of an OLED device here we will simulate a simpler single-carrier device, which is shown schematically in Figure 9a. The experimental measurements (Section 7) are also performed using this setup.

### 6.1. Drift-Diffusion Modeling

The drift-diffusion model assumes that local charge density,  $\rho(x)$ , charge mobility,  $\mu(x; \rho, F, T)$ , field strength,  $F(x)$ , and diffusion constant,  $D(x; \rho, F, T)$ , are changing continuously. In one dimension, the corresponding drift-diffusion equation then reads

$$J = q\rho\mu + qD \frac{\partial \rho}{\partial x} \quad (11)$$

Here the first (drift) term describes transport of holes/electrons in/against the direction of the electric field. The second (diffusion) term is due to transport of charges against the gradient of charge density.

The drift-diffusion equation is complemented by Gauss's law,  $\partial F(x)/\partial x = \rho(x)/\epsilon$ , where  $\epsilon$  is the relative permittivity. The dependence of mobility on charge density, electric field, and temperature can be obtained from Monte Carlo simulations as described in Section 4.  $\mu$  and  $D$  are related via the generalized Einstein equation.<sup>[120]</sup> Boundary conditions fix the charge carrier density at the electrodes,  $\rho_{\text{el}}$ , to the value given by a thermal equilibrium between the electrode and the organic layer

$$\rho_{\text{el}} = \int_{-\infty}^{\infty} \frac{g(E)}{1 + \exp\left[\frac{E + \Delta}{k_{\text{B}}T}\right]} dE \quad (12)$$

where  $g(E)$  is the density of states.

To correct for the presence of the image potential, an equilibrium between the Fermi level of the injecting electrode and the maximum of the sum of the applied driving bias, the local potential as obtained from the Poisson equation and the image potential is assumed. The lowering of the injection barrier,  $\Delta$ , between the Fermi level of the electrode and of the organic site is then described by<sup>[121]</sup>

$$\Delta' = \Delta - q\sqrt{\frac{qF_{\text{c}}}{4\pi\epsilon}} \quad (13)$$

The field at the electrode,  $F_{\text{c}}$ , and the lowering of the injection barrier,  $\Delta'$ , are determined self-consistently via an iterative procedure.<sup>[122]</sup> When the field at the electrode is directed into the electrode itself, i.e.,  $F_{\text{c}} < 0$ , the injection barrier is not lowered by the image potential. Before solving the drift-diffusion equation we have parametrized the field and temperature dependencies of the mobility, as described in Section 4, i.e., fitted the results of Monte Carlo simulations performed in an amorphous morphology of 4000 DPBIC molecules to the EGDM. Lattice spacing, energetic disorder, and zero-field mobility were used as fit parameters and are summarized in Table 1. The drift-diffusion equations were then solved for several values of the injection barrier,  $\Delta$ , and are shown in Figure 8a. Up to  $\Delta = 0.2$  eV the *IV* curves are practically on top of each other. Only from 0.4 eV the injection barrier starts to affect the *IV* characteristics. One can also see that for larger values of  $\Delta$  (less effective injection) the current density decreases by several orders of magnitude.

Drift-diffusion equations, combined with the EGDM and ECDM models, are often used for fitting to experimentally measured *IV* characteristics, in order to characterize a particular material. The results of such a fit, are summarized in Table 1. Here we performed a simultaneous fit to nine different *IV* curves, measured using three layer thicknesses (108, 162, 219 nm) and three temperatures (233, 293, 313 K). The model includes a fitted injection barrier (0.05 eV) and doped injection layers which provide the (almost) Ohmic injection, similar to the experimental setup shown in Figure 9a.

Since in organic materials the transport of charge carriers is percolative and the current density in the device has a filamentary structure,<sup>[123–125]</sup> it is not immediately clear how reliable drift-diffusion device models are.<sup>[126]</sup> This is addressed in the next section by comparing the drift-diffusion solution to the results of lattice simulations.

### 6.2. Lattice Monte Carlo

To be able to use the Monte Carlo procedure for devices, additional sites, which play the role of electrodes, are added. The injection/collection of a charge carrier to/from the electrode is modeled as a hopping of this charge carrier between the electrode and the lattice site to/from which the charge carrier is injected/collected.<sup>[97,126]</sup>

Additional contributions to site energies (due to electrodes) include a linear drop in the applied potential,  $eV(1-x/L)$ . Here the Fermi energy of the electron injecting electrode ( $x = L$ )

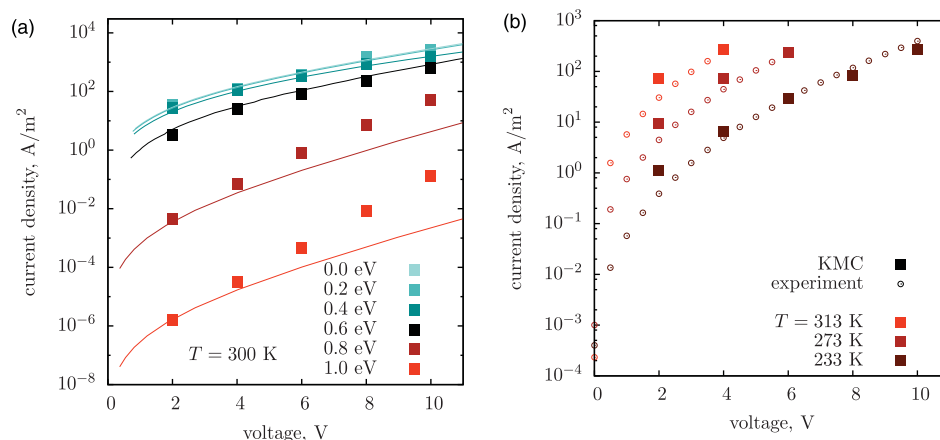


**Figure 8.** a) Simulated current–voltage characteristics of a single-carrier device with electrodes. Squares show the results of Monte Carlo simulations in a cubic lattice, which are compared to drift-diffusion simulations (solid lines) using the EGDM mobility parametrized on a microscopic system. Different colors correspond to different values of the injection barrier  $\Delta$ . b) Current–voltage characteristics of the off-lattice (coarse-grained) model obtained by Monte Carlo simulations (squares) and measured experimentally (circles) for three different temperatures.

is taken as a reference, while the applied potential at the collecting electrode is set to  $V$ . An injection barrier,  $\Delta$ , is introduced between the Fermi level of the electrode and the one of the sites of organic material, such that the energy difference to the electrode is raised by  $\Delta$ ,  $E_{el,i} = -E_{el} + E_i + \Delta$ , while for the charge transfer into the electrode  $E_{i,el} = E_{el} - E_i - \Delta$ . These contributions are depicted in Figure 9d.

Coulomb interactions are split into a short-range and a long-range contribution. The short-range part is evaluated explicitly for all charges (and their periodic images) within separations smaller than  $r_c$ . Between one and ten images provide sufficient accuracy, such that a computationally demanding Ewald summation can be avoided.

The long-range contribution is evaluated by first calculating the local charge carrier density,  $\rho(x)$ , by averaging the number

of charges in two-dimensional ( $yz$ ) slabs oriented perpendicular to the electric field direction (along the  $x$  axis). Then the electrostatic potential,  $\varphi(x)$ , is reconstructed using the Poisson equation,  $\varphi''(x) = -\rho(x)/\epsilon$ . Note that the layer-averaged potential also takes into account the short-range interactions and one needs to correct for this double counting.

The current density throughout the device is evaluated as

$$J = \frac{q \sum_k \Delta \mathbf{r}_k \cdot \mathbf{F}}{A \tau F} \quad (14)$$

where  $\Delta \mathbf{r}_k \cdot \mathbf{F}/F$  is the change in position of a charge along the applied field  $\mathbf{F}$ ,  $A$  is the surface area of the electrodes, and  $\tau$  is the total simulated time.

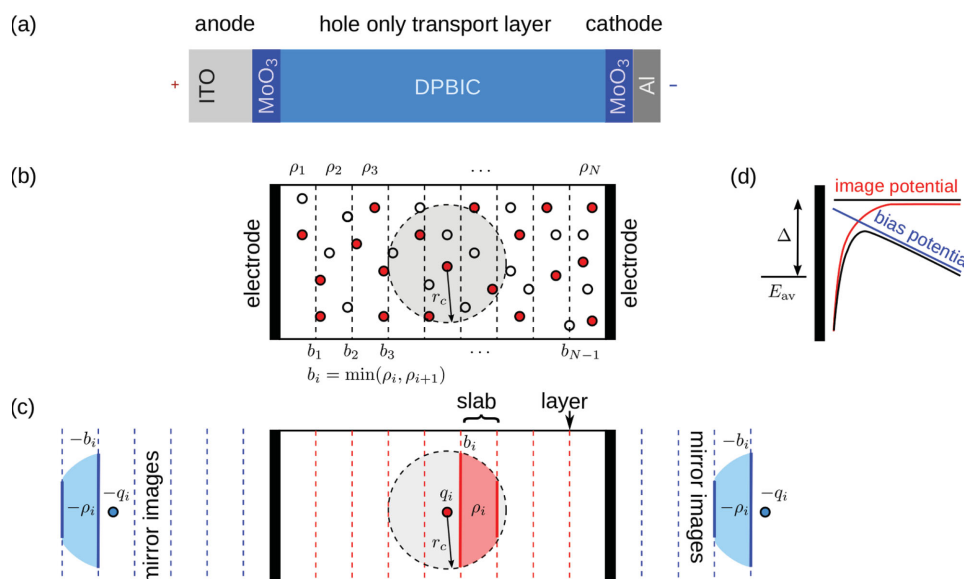


**Figure 9.** a) Experimental setup for single-carrier-type measurements, here of the DPBIC hole-conduction layer. b) Simulation setup mimicking the device. c) Evaluation of the long- and short-range electrostatic contributions in device geometry. d) Additional contributions to site energies due to electrodes: a linear drop in the applied potential and an injection barrier  $\Delta$ .

Apart from device simulations, the lattice Monte Carlo method can be used to benchmark the accuracy of the continuum drift-diffusion solver, discussed in Section 6.1. Figure 8a shows *IV* curves obtained by Monte Carlo simulations in a cubic lattice with lattice spacing  $a = 1.67$  nm and Gaussian-distributed site energies of width  $\sigma = 0.134$  eV, i.e., the same parameters as in the EGDM mobility parametrization, see Section 4. One can see that lattice Monte Carlo results agree reasonably well with the EGDM model combined with the drift-diffusion solver. Note that at low voltages (small drift currents) the KMC algorithm converges very slowly, which is why we have included KMC results only for voltages higher than 2 V.

### 6.3. Off-Lattice Monte Carlo

The Monte Carlo scheme on a lattice can be generalized to off-lattice models, thus helping to avoid parametrizations of mobility as well as assumptions incorporated in lattice models. Again, the effects that need to be taken into account are Coulomb interactions and the injection from the electrodes into the organic layer. To model the injection process, an electronic coupling of the form  $J_{inj} = \exp(-2\alpha r_{ij})$  is assumed between the electrodes and the organic material, where  $\alpha$  is the inverse wavefunction decay length and  $r_{ij}$  is the distance between the electrode and the site to or from which the charge carrier is injected or collected. This introduces two parameters,  $\alpha$  and  $d$ , where the latter is the distance between the electrode and the organic site nearest to that electrode. Close to the electrodes the image charge effect leads to an effective lowering of the energetic disorder.<sup>[127]</sup> This is accounted for by a factor  $\gamma$  which rescales the site energy,  $E_i$ , of injection/collection sites to  $E'_i = \gamma(E_i - \langle E_i \rangle) + \langle E_i \rangle$ , where  $\langle E_i \rangle$  is the average site energy.

Coulomb interactions are split into a short-range and a long range contribution. The short-range part is evaluated in a similar way as for the lattice, except that ten to hundred images are included to improve accuracy. For the long-range part the total simulation box is split into three-dimensional slabs of equal thickness, as shown in Figure 9b. All charges in a slab are summed up to obtain the slab-averaged charge carrier density,  $\rho_i$ . The slab-averaged potential,  $\phi(x)$ , is then evaluated by solving the Poisson equation, where the slab-averaged charge carrier densities are used as a source term. Again, similar to the lattice Monte Carlo, the layer-averaged potential already takes into account short-range interactions. Thus double counting should be corrected for, as shown in Figure 9c. The computationally expensive update of the averaged long-range potential and the re-evaluation of the hopping rates is done every 100–1000 hops, which yields sufficient accuracy of long-range effects.

To perform charge transport simulations, we used the coarse-grained off-lattice model of DPBIC, parametrized as discussed in Section 3. An amorphous morphology of 255 083 molecules was generated in a box of  $123 \times 50 \times 50$  nm<sup>3</sup> to match the experimentally used layer thickness (see Section 7 for details). Periodic boundary conditions were employed in the directions perpendicular to the electric field. The simulated *IV* curves, together with the experimental data points are shown in Figure 8b for  $\alpha = 13$  nm<sup>-1</sup>,  $d = 0.5$  nm,  $\Delta = 0.5$  eV, and  $\gamma = 0.55$ , and are in good agreement with each other.

## 7. Experimental Section

In order to decouple different processes in OLEDs, experiments are often performed in single-layer hole-only or electron-only devices.<sup>[128]</sup> Here we used a setup shown in Figure 9a with 5 nm molybdenum trioxide (MoO<sub>3</sub>) layers on both sides of a 123 nm DPBIC layer. The function of the MoO<sub>3</sub> layers is to allow band bending,<sup>[129]</sup> resulting in an (almost) Ohmic injection to the DPBIC layer.<sup>[130]</sup>

The devices were fabricated by vacuum thermal evaporation of the organic material on a glass substrate patterned with a 140 nm thick indium tin oxide (ITO) layer as an anode. Prior to deposition, substrates were cleaned in an ultrasonic bath using subsequently detergents and de-ionized water. The samples were dried and treated in an ozone oven to additionally clean them and modify the ITO work function. A 100 nm film of thermally evaporated aluminum (Al) is used as a cathode. In order to exactly determine the thickness of the DPBIC layer, we simultaneously deposited the same amount of DPBIC on a silicon wafer, mounted adjacent to the substrate and measured its thickness using optical ellipsometry.

The fabricated samples were placed into the oil reservoir of a cryostat, where the temperature was varied between 233 and 313 K. The experimentally measured *IV* curves are shown in Figure 8 for three different temperatures, together with simulation results described in Section 6.

## 8. Materials

To this end, we have simulated current–voltage characteristics of a diode with a hole-conducting DPBIC used as organic layer. While this example is so far the only exhaustive illustration of multiscale simulations techniques which can be used to simulate charge transport in disordered organic semiconductors, a number of similar methods have already been used to evaluate material properties of such materials.<sup>[16,17]</sup> Here we will provide a (far from complete) review of such case studies. In particular, we will focus on charge transport in amorphous mesophases of DPBIC, BTDF, TBFMI, BCP,  $\alpha$ -NPD, and Alq3, chemical structures of which are shown in Figure 10.

**DPBIC:** Tris[(3-phenyl-1H-benzimidazol-1-yl-2(3H)-ylidene)-1,2-phenylene]Ir is used in OLEDs as a hole-transporting and electron-blocking material.<sup>[131–134]</sup> Apart from *IV* dependencies discussed here, simulations of amorphous DPBIC predict a density value of 1.29 g cm<sup>-3</sup> and an energetic disorder of 0.176 eV, which compares reasonably well to the experimentally determined value of 0.121 eV, that relies on the ECDM.<sup>[28]</sup> In amorphous morphology the perturbative approach yields an ionization potential (IP) of 5.28 eV, in perfect agreement with the Conductor-like screening model (COSMO)<sup>[135]</sup> giving the same value of 5.28 eV. Both the Poole–Frenkel dependence and the absolute value of mobility are in agreement with experimental measurements: For small fields the simulated hole mobility varies from  $6.6 \times 10^{-10}$  m<sup>2</sup> V<sup>-1</sup> s<sup>-1</sup> ( $\rho = 4.25 \times 10^{23}$  m<sup>-3</sup>) to  $3.6 \times 10^{-8}$  m<sup>2</sup> V<sup>-1</sup> s<sup>-1</sup> ( $\rho = 1.36 \times 10^{25}$  m<sup>-3</sup>), while the experimental value is  $9 \times 10^{-9}$  m<sup>2</sup> V<sup>-1</sup> s<sup>-1</sup>.

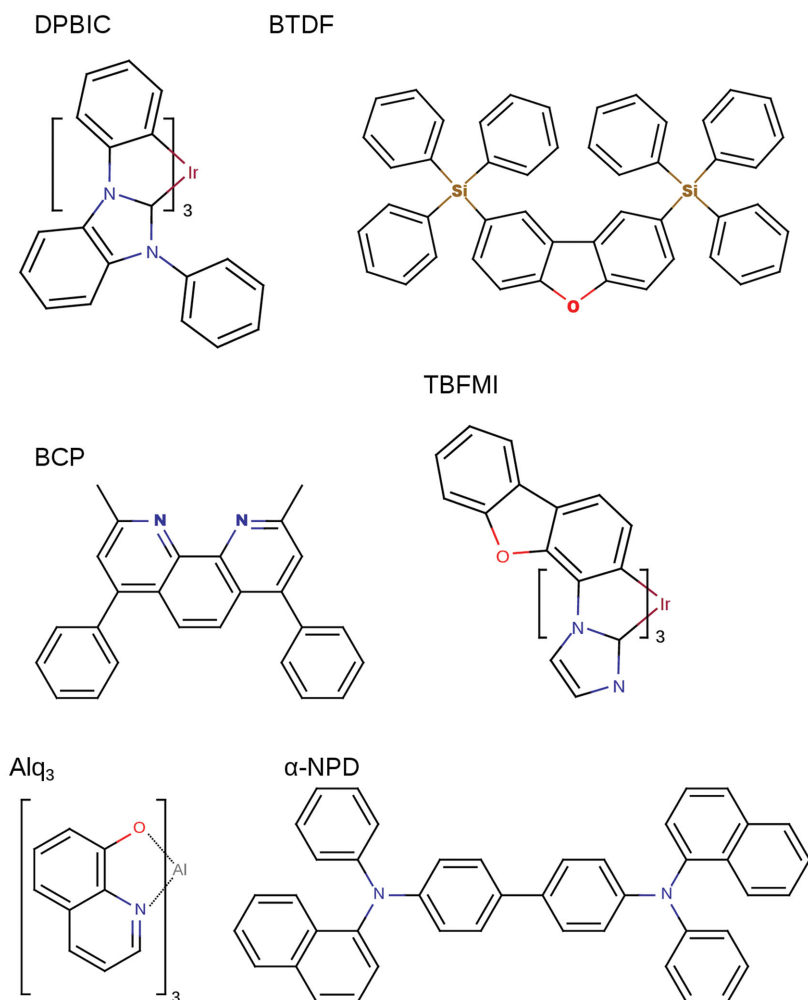


Figure 10. Chemical structures of materials used in OLEDs.

**BTDF:** 8-bis(triphenylsilyl)-dibenzofuran (BTDF) is an electron-conducting and hole-blocking material<sup>[131]</sup> which, in combination with a deep blue emitter, can lead to quantum efficiencies above 17%.<sup>[20]</sup> Its glass transition temperature is at 107 °C.<sup>[20]</sup> Molecular dynamics simulations predict an amorphous density of 1.37 g cm<sup>-3</sup>.<sup>[20]</sup> Calculations based on polarizable force-fields predict an energetic disorder of  $\sigma = 0.085$  eV (electrons) and  $\sigma = 0.078$  eV (holes). Simulated in the zero-charge density limit mobilities,  $1.0 \times 10^{-9}$  m<sup>2</sup> V<sup>-1</sup> s<sup>-1</sup> for holes and  $3.2 \times 10^{-8}$  m<sup>2</sup> V<sup>-1</sup> s<sup>-1</sup> for electrons, are comparable to the experimental values obtained using admittance spectroscopy,  $2.5 \times 10^{-10}$  m<sup>2</sup> V<sup>-1</sup> s<sup>-1</sup> for holes and  $1.0 \times 10^{-8}$  m<sup>2</sup> V<sup>-1</sup> s<sup>-1</sup> for electrons, measured at an electric field of  $9 \times 10^6$  V m<sup>-1</sup> (holes)  $3 \times 10^7$  V m<sup>-1</sup> (electrons).

**TBFMI:** Tris[(1,2-dibenzofurane-4-ylidene)(3-methyl-1H-imidazole-5-ylidene)]Ir(III) (TBFMI) has been used as an emitter molecule in various host-guest mixtures, for example, with BTDF. An important quantity in such mixtures is the relative alignment of densities of states of the host and guest

materials. For example, in TBFMI:BTDF the energy offset between the host and the guest is very small, which is mostly due to environmental effects. In particular, the change in molecular polarizability upon charging plays an important role.<sup>[21]</sup>

**BCP:** 2,9-dimethyl-4,7-diphenyl-1,10-phenanthroline (bathocuproine, BCP) is a typical electron conducting and hole blocking material which is used in phosphorescent OLEDs.<sup>[136–140]</sup> Simulations of charge transport in a crystalline phase of this material,<sup>[140]</sup> using a model based on quantum mechanic calculations of a sample dimer, show mobilities of  $1.8 \times 10^{-6}$  m<sup>2</sup> V<sup>-1</sup> s<sup>-1</sup> in a reasonable agreement with a reported experimental value of  $1.1 \times 10^{-7}$  m<sup>2</sup> V<sup>-1</sup> s<sup>-1</sup>.<sup>[141]</sup>

**$\alpha$ -NPD:** N,N'-bis(1-naphthyl)-N,N'-diphenyl-1,1'-biphenyl-4,4'-diamine ( $\alpha$ -NPD or NPB) can be used in OLEDs as a hole-transporting, electron-blocking,<sup>[138,142–146]</sup> or blue-emitting layer,<sup>[147,148]</sup> and as a host material.<sup>[149,150]</sup> It has a relatively high glass transition temperature of 95 °C, favorable for the material's stability. In the amorphous phase, a density of 1.16 g cm<sup>-3</sup> has been reported from X-ray reflectometry measurements.<sup>[151]</sup> IV curves in an  $\alpha$ -NPD based diode were simulated by solving the drift-diffusion equations using both extended and correlated Gaussian disorder models. Both models provide a consistent description of the IV characteristics at different temperatures. However, the lattice constant obtained from the ECDM fit is closer to the experimentally known intersite distance, i.e., spatial correlations of site energies in this material are important. The amorphous

morphology of  $\alpha$ -NPD has been studied by using the Monte Carlo algorithm that mimics the vacuum deposition process<sup>[44]</sup> as well as by MD simulations.<sup>[152]</sup> The latter, combined with electrostatic and induction calculations, gave energetic disorder values of  $\sigma = 0.09–0.11$  eV (electrons) and  $\sigma = 0.14–0.15$  eV (holes). Simulated mobilities, obtained by applying an analytic solution of the master equation to the transport network, varied from  $4.2 \times 10^{-10}$  to  $1.3 \times 10^{-9}$  m<sup>2</sup> V<sup>-1</sup> s<sup>-1</sup> (holes) and from  $1.1 \times 10^{-6}$  to  $4.1 \times 10^{-6}$  m<sup>2</sup> V<sup>-1</sup> s<sup>-1</sup> (electrons), in good agreement with the experimentally measured value of  $7.8 \times 10^{-10}$  m<sup>2</sup> V<sup>-1</sup> s<sup>-1</sup> for holes.<sup>[153]</sup>

**Alq3:** Mer-tris(8-hydroxyquinolato)aluminum (Alq3) was used in the first organic diode already in 1987<sup>[154]</sup> and ever since has been studied intensively. The amorphous morphology of Alq3, obtained by annealing above the glass transition temperature and subsequent cool-down<sup>[34]</sup> to room temperature, resulted in density of 1.18 g cm<sup>-3</sup> (Williams 99 force field) and 1.29 g cm<sup>-3</sup> (OPLS force field), while Monte Carlo-based vacuum-deposition algorithm with the local relaxation after deposition led to 1.22 g cm<sup>-3</sup> (OPLS force field).<sup>[44]</sup> Experimentally

reported values range from  $1.3 \text{ g cm}^{-3}$ <sup>[155]</sup> to  $1.5 \text{ g cm}^{-3}$ .<sup>[156]</sup> Simulations predict energetic disorder of 0.21 eV for holes.<sup>[17]</sup> Charge transport simulations have shown that spatial correlation of site energies is responsible for the Poole–Frenkel behavior of the charge mobility<sup>[17]</sup> and that finite-size effects should be carefully accounted for in systems with large energetic disorder.<sup>[35]</sup>

## 9. Conclusions and Outlook

We have reviewed a set of simulation techniques used to understand charge transport in amorphous organic materials. The distinct feature of these techniques is that they all start with chemical structures and predict, by building a hierarchical set of models, macroscopic properties of devices, in our case charge carrier mobility and current–voltage characteristics of an organic light emitting diode. The advantages and shortcomings of all techniques have been illustrated by simulating (and validating experimentally) charge dynamics in a unipolar device with a hole conducting material used in state of the art diodes. We have also identified areas where substantial method development is still required in order to achieve a parameter-free modeling of realistic devices. In particular, still missing are (i) first-principles evaluations of charge injection rates (from metal to organic material), (ii) explicit treatment of the induction interaction when solving the master equation (re-evaluation of rates at every Monte Carlo step), (iii) quantitative treatment of excited states embedded in a heterogeneous polarizable molecular environment, (iv) descriptions of charge–exciton and exciton–exciton interactions. Advancements in all these directions are absolutely vital for devising accurate structure–property relationships for organic semiconductors.

## Acknowledgements

This work was in part supported by the DFG (Program No. IRTG 1404), DFG (Grant No. SPP 1355), and BMBF (Grant Nos. MEDOS (FKZ 03EK3503B) and MESOMERIE (FKZ 13N10723)). We are grateful to Carl Poelking, Anton Melnyk, Jens Wehner, and Kurt Kremer for a critical reading of the manuscript.

Received: August 31, 2014

Revised: November 13, 2014

Published online: January 3, 2015

- [1] C. Chiang, C. Fincher, Y. Park, A. Heeger, H. Shirakawa, E. Louis, S. Gau, A. MacDiarmid, *Phys. Rev. Lett.* **1977**, *39*, 1098.
- [2] A. Tsumura, H. Kozuka, T. Ando, *Appl. Phys. Lett.* **1986**, *49*, 1210.
- [3] S. R. Forrest, *Nature* **2004**, *428*, 911.
- [4] C. W. Tang, *Appl. Phys. Lett.* **1986**, *48*, 183.
- [5] R. Parashkov, E. Becker, T. Riedl, H.-H. Johannes, W. Kowalsky, *Proc. IEEE* **2005**, *93*, 1321.
- [6] P.-L. T. Boudreault, A. Najari, M. Leclerc, *Chem. Mater.* **2011**, *23*, 456.
- [7] E. Bundgaard, F. Krebs, *Solar Energy Mater. Solar Cells* **2007**, *91*, 954.
- [8] Y. Shirota, H. Kageyama, *Chem. Rev.* **2007**, *107*, 953.
- [9] S. Reineke, F. Lindner, G. Schwartz, N. Seidler, K. Walzer, B. Lüssem, K. Leo, *Nature* **2009**, *459*, 234.
- [10] T. D. Schmidt, B. J. Scholz, C. Mayr, W. Bruetting, *IEEE J. Sel. Top. Quantum Electron.* **2013**, *19*, 1.
- [11] C. Tanase, E. J. Meijer, P. W. M. Blom, D. M. de Leeuw, *Phys. Rev. Lett.* **2003**, *91*, 216601.
- [12] P. Blom, M. De Jong, *IEEE J. Sel. Top. Quantum Electron.* **1998**, *4*, 105.
- [13] E. J. Meijer, C. Tanase, P. W. M. Blom, E. van Veenendaal, B.-H. Huisman, D. M. de Leeuw, T. M. Klapwijk, *Appl. Phys. Lett.* **2002**, *80*, 3838.
- [14] S. Athanasopoulos, J. Kirkpatrick, D. Martínez, J. M. Frost, C. M. Foden, A. B. Walker, J. Nelson, *Nano Lett.* **2007**, *7*, 1785.
- [15] J. Kirkpatrick, V. Marcon, J. Nelson, K. Kremer, D. Andrienko, *Phys. Rev. Lett.* **2007**, *98*, 227402.
- [16] J. Nelson, J. J. Kwiatkowski, J. Kirkpatrick, J. M. Frost, *Acc. Chem. Res.* **2009**, *42*, 1768.
- [17] V. Rühle, A. Lukyanov, F. May, M. Schrader, T. Vehoff, J. Kirkpatrick, B. Baumeier, D. Andrienko, *J. Chem. Theory Comput.* **2011**, *7*, 3335.
- [18] M. Schrader, R. Fitzner, M. Hein, C. Elschner, B. Baumeier, K. Leo, M. Riede, P. Baeuerle, D. Andrienko, *J. Am. Chem. Soc.* **2012**, *134*, 6052.
- [19] M. Schrader, C. Körner, C. Elschner, D. Andrienko, *J. Mater. Chem.* **2012**, *22*, 22258.
- [20] F. May, M. Al-Helwi, B. Baumeier, W. Kowalsky, E. Fuchs, C. Lennartz, D. Andrienko, *J. Am. Chem. Soc.* **2012**, *134*, 13818.
- [21] F. May, B. Baumeier, C. Lennartz, D. Andrienko, *Phys. Rev. Lett.* **2012**, *109*, 136401.
- [22] C. Poelking, D. Andrienko, *Macromolec.* **2013**, *46*, 8941.
- [23] C. Poelking, E. Cho, A. Malafeev, V. Ivanov, K. Kremer, C. Risko, J.-L. Brédas, D. Andrienko, *J. Phys. Chem. C* **2013**, *117*, 1633.
- [24] P. Borsenberger, L. Pautmeier, H. Bässler, *J. Chem. Phys.* **1991**, *94*, 5447.
- [25] H. Bässler, *Phys. Status Solidi B* **1993**, *175*, 15.
- [26] S. Novikov, D. Dunlap, V. Kenkre, P. Parris, A. Vannikov, *Phys. Rev. Lett.* **1998**, *81*, 4472.
- [27] W. F. Pasveer, J. Cottaar, C. Tanase, R. Coehoorn, P. A. Bobbert, P. W. M. Blom, D. M. de Leeuw, M. A. J. Michels, *Phys. Rev. Lett.* **2005**, *94*, 206601.
- [28] M. Bouhassoune, S. v. Mensfoort, P. Bobbert, R. Coehoorn, *Org. Electron.* **2009**, *10*, 437.
- [29] P. Kordt, O. Stenzel, B. Baumeier, V. Schmidt, D. Andrienko, *J. Chem. Theory Comput.* **2014**, *10*, 2508.
- [30] B. Baumeier, O. Stenzel, C. Poelking, D. Andrienko, V. Schmidt, *Phys. Rev. B* **2012**, *86*, 184202.
- [31] P. Strohriegel, D. Wagner, P. Schrögel, S. T. Hoffmann, A. Köhler, U. Heinemeyer, I. Münster, *Proc. SPIE* **2013**, *8829*, 882906.
- [32] A. J. Stone, *The Theory of Intermolecular Forces*, Clarendon Press, Oxford **1997**.
- [33] J. J. Kwiatkowski, J. Nelson, H. Li, J. L. Bredas, W. Wenzel, C. Lennartz, *Phys. Chem. Chem. Phys.* **2008**, *10*, 1852.
- [34] A. Lukyanov, C. Lennartz, D. Andrienko, *Phys. Status Solidi A* **2009**, *206*, 2737.
- [35] A. Lukyanov, D. Andrienko, *Phys. Rev. B* **2010**, *82*, 193202.
- [36] J. J. Kwiatkowski, J. M. Frost, J. Nelson, *Nano Lett.* **2009**, *9*, 1085.
- [37] R. C. I. MacKenzie, J. M. Frost, J. Nelson, *J. Chem. Phys.* **2010**, *132*, 064904.
- [38] C. Elschner, M. Schrader, R. Fitzner, A. A. Levin, P. Bäuerle, D. Andrienko, K. Leo, M. Riede, *RSC Adv.* **2013**, *3*, 12117.
- [39] X. L. Feng, V. Marcon, W. Pisula, M. R. Hansen, J. Kirkpatrick, F. Grozema, D. Andrienko, K. Kremer, K. Müllen, *Nat. Mater.* **2009**, *8*, 421.
- [40] V. Marcon, T. Vehoff, J. Kirkpatrick, C. Jeong, D. Y. Yoon, K. Kremer, D. Andrienko, *J. Chem. Phys.* **2008**, *129*, 094505.

- [41] F. May, V. Marcon, M. R. Hansen, F. Grozema, D. Andrienko, *J. Mater. Chem.* **2011**, *21*, 9538.
- [42] T. Vehoff, J. Kirkpatrick, K. Kremer, D. Andrienko, *Phys. Status Solidi B* **2008**, *245*, 839.
- [43] R. S. Bhatta, Y. Y. Yimer, D. S. Perry, M. Tsige, *J. Phys. Chem. B* **2013**, *117*, 10035.
- [44] T. Neumann, D. Danilov, C. Lennartz, W. Wenzel, *J. Comput. Chem.* **2013**, *34*, 2716.
- [45] L. Muccioli, G. D'Avino, R. Berardi, S. Orlandi, A. Pizzirusso, M. Ricci, O. M. Roscioni, C. Zannoni, *Supramolecular Organization of Functional Organic Materials in the Bulk and at Organic/Organic Interfaces: A Modeling and Computer Simulation Approach*, Topics in Current Chemistry, Springer, Berlin **2013**, pp. 1–63.
- [46] L. Muccioli, G. D'Avino, C. Zannoni, *Adv. Mater.* **2011**, *23*, 4532.
- [47] H. J. C. Berendsen, J. P. M. Postma, W. F. v. Gunsteren, A. DiNola, J. R. Haak, *J. Chem. Phys.* **1984**, *81*, 3684.
- [48] G. C. Cho, A. Ziebell, T. Dekorsy, H. J. Bakker, B. Opitz, A. Kohl, H. Kurz, *J. Appl. Phys.* **1997**, *82*, 4400.
- [49] K. Hannewald, P. A. Bobbert, *Appl. Phys. Lett.* **2004**, *85*, 1535.
- [50] F. Ortman, F. Bechstedt, K. Hannewald, *Phys. Status Solidi B* **2011**, *248*, 511.
- [51] W. Warta, R. Stehle, N. Karl, *Appl. Phys. A* **1985**, *36*, 163.
- [52] J.-D. Picon, M. N. Bussac, L. Zuppiroli, *Phys. Rev. B* **2007**, *75*, 235106.
- [53] A. Troisi, G. Orlandi, *Phys. Rev. Lett.* **2006**, *96*, 086601.
- [54] A. Troisi, D. L. Cheung, D. Andrienko, *Phys. Rev. Lett.* **2009**, *102*, 116602.
- [55] H. Bäessler, A. Köhler, in *Unimolecular and Supramolecular Electronics I* (Ed: R. M. Metzger), Topics in Current Chemistry, Vol. 312, Springer, Berlin **2012**, pp. 1–65.
- [56] R. Fornari, A. Troisi, *Phys. Chem. Chem. Phys.* **2014**, *16*, 9997.
- [57] C. Poelking, K. Daoulas, A. Troisi, D. Andrienko, *Morphology and Charge Transport in P3HT: A Theorist's Perspective*, Advances in Polymer Science, Springer, Berlin **2014**, pp. 1–42.
- [58] R. A. Marcus, *Rev. Mod. Phys.* **1993**, *65*, 599.
- [59] G. R. Hutchison, M. A. Ratner, T. J. Marks, *J. Am. Chem. Soc.* **2005**, *127*, 2339.
- [60] V. May, O. Kühn, *Charge and Energy Transfer Dynamics in Molecular Systems*, Wiley-VCH, Weinheim, Germany **2011**.
- [61] M. Bixon, J. Jortner, in *Advances in Chemical Physics* (Eds: I. Prigogine, S. A. Rice), John Wiley & Sons, Inc., Hoboken **2007**, pp. 35–202.
- [62] R. Egger, C. H. Mak, U. Weiss, *J. Chem. Phys.* **1994**, *100*, 2651.
- [63] M. P. A. Fisher, A. T. Dorsey, *Phys. Rev. Lett.* **1985**, *54*, 1609.
- [64] H. Grabert, U. Weiss, *Phys. Rev. Lett.* **1985**, *54*, 1605.
- [65] K. Asadi, A. J. Kronemeijer, T. Cramer, L. Jan Anton Koster, P. W. M. Blom, D. M. de Leeuw, *Nat. Commun.* **2013**, *4*, 1710.
- [66] A. Stone, M. Alderton, *Mol. Phys.* **1985**, *56*, 1047.
- [67] B. T. Thole, *Chem. Phys.* **1981**, *59*, 341.
- [68] P. T. van Duijnen, M. Swart, *J. Phys. Chem. A* **1998**, *102*, 2399.
- [69] P. Ren, J. W. Ponder, *J. Phys. Chem. B* **2003**, *107*, 5933.
- [70] C. Poelking, M. Tietze, C. Elschner, S. Olthof, D. Hertel, B. Baumeier, F. Würthner, K. Meerholz, K. Leo, D. Andrienko, *Nat. Mater.*, DOI: 10.1038/NMAT4167.
- [71] P. P. Ewald, *Ann. Phys.* **1921**, *369*, 253.
- [72] E. R. Smith, *Proc. R. Soc. London, Ser. A* **1981**, *375*, 475.
- [73] S. V. Novikov, A. V. Vannikov, *J. Phys. Chem.* **1995**, *99*, 14573.
- [74] J.-L. Brédas, D. Beljonne, V. Coropceanu, J. Cornil, *Chem. Rev.* **2004**, *104*, 4971.
- [75] D. P. McMahon, A. Troisi, *J. Phys. Chem. Lett.* **2010**, *1*, 941.
- [76] J. E. Norton, J.-L. Brédas, *J. Am. Chem. Soc.* **2008**, *130*, 12377.
- [77] B. Baumeier, J. Kirkpatrick, D. Andrienko, *Phys. Chem. Chem. Phys.* **2010**, *12*, 11103.
- [78] J. Huang, M. Kertesz, *J. Chem. Phys.* **2005**, *122*, 234707.
- [79] E. F. Valeev, V. Coropceanu, D. A. da Silva Filho, S. Salman, J.-L. Brédas, *J. Am. Chem. Soc.* **2006**, *128*, 9882.
- [80] T. Van Voorhis, T. Kowalczyk, B. Kaduk, L.-P. Wang, C.-L. Cheng, Q. Wu, *Annu. Rev. Phys. Chem.* **2010**, *61*, 149.
- [81] J. Ridley, M. Zerner, *Theor. Chim. Acta* **1973**, *32*, 111.
- [82] V. Coropceanu, J. Cornil, D. A. da Silva Filho, Y. Olivier, R. Silbey, J.-L. Brédas, *Chem. Rev.* **2007**, *107*, 926.
- [83] J. Kirkpatrick, *Int. J. Quantum Chem.* **2008**, *108*, 51.
- [84] T. Vehoff, Y. S. Chung, K. Johnston, A. Troisi, D. Y. Yoon, D. Andrienko, *J. Phys. Chem. C* **2010**, *114*, 10592.
- [85] T. Vehoff, B. Baumeier, D. Andrienko, *J. Chem. Phys.* **2010**, *133*, 134901.
- [86] A. Kubas, F. Hoffmann, A. Heck, H. Oberhofer, M. Elstner, J. Blumberger, *J. Chem. Phys.* **2014**, *140*, 104105.
- [87] F. Gajdos, S. Valner, F. Hoffmann, J. Spencer, M. Breuer, A. Kubas, M. Dupuis, J. Blumberger, *J. Chem. Theory Comput.*, DOI: 10.1021/ct500527v.
- [88] T. Brereton, O. Stenzel, B. Baumeier, D. Andrienko, V. Schmidt, D. Kroese, *Methodol. Comput. Appl. Probab.* **2014**, *16*, 465.
- [89] O. Stenzel, C. Hirsch, T. Brereton, B. Baumeier, D. Andrienko, D. Kroese, V. Schmidt, *Multiscale Model. Simul.* **2014**, *12*, 1108.
- [90] W. Tschöp, K. Kremer, J. Batoulis, T. Bürger, O. Hahn, *Acta Polym.* **1998**, *49*, 61.
- [91] D. Reith, M. Pütz, F. Müller-Plathe, *J. Comput. Chem.* **2003**, *24*, 1624.
- [92] A. P. Lyubartsev, A. Laaksonen, *Phys. Rev. E* **1995**, *52*, 3730.
- [93] A. K. Soper, *Chem. Phys.* **1996**, *202*, 295.
- [94] T. Murtola, A. Bunker, I. Vattulainen, M. Deserno, M. Karttunen, *Phys. Chem. Chem. Phys.* **2009**, *11*, 1869.
- [95] R. L. Henderson, *Phys. Lett. A* **1974**, *49*, 197.
- [96] V. Rühle, C. Junghans, A. Lukyanov, K. Kremer, D. Andrienko, *J. Chem. Theory Comput.* **2009**, *5*, 3211.
- [97] J. J. M. van der Holst, F. W. A. van Oost, R. Coehoorn, P. A. Bobbert, *Phys. Rev. B* **2011**, *83*, 085206.
- [98] J. Honerkamp, *Stochastische Dynamische Systeme: Konzepte, Numerische Methoden, Datenanalysen*, VCH, Weinheim, Germany **1990**.
- [99] D. T. Gillespie, *J. Comput. Phys.* **1976**, *22*, 403.
- [100] D. T. Gillespie, *J. Phys. Chem.* **1977**, *81*, 2340.
- [101] J. Cottaar, P. A. Bobbert, *Phys. Rev. B* **2006**, *74*, 115204.
- [102] N. W. Ashcroft, *Solid State Physics*, Holt, Rinehart and Winston, New York **1976**.
- [103] T. Hanney, M. R. Evans, *J. Stat. Phys.* **2003**, *111*, 1377.
- [104] A. V. Nenashev, F. Jansson, S. D. Baranovskii, R. Österbacka, A. V. Dvurechenskii, F. Gebhard, *Phys. Rev. B* **2010**, *81*, 115203.
- [105] N. G. Van Kampen, *J. Phys. Chem. Solids* **1988**, *49*, 673.
- [106] M. Christensen, J. B. Pedersen, *J. Chem. Phys.* **2003**, *119*, 5171.
- [107] K. A. Fichthorn, W. H. Weinberg, *J. Chem. Phys.* **1991**, *95*, 1090.
- [108] A. P. J. Jansen, *Comput. Phys. Commun.* **1995**, *86*, 1.
- [109] H. A. Simon, A. Ando, *Econometrica* **1961**, *29*, 111.
- [110] S. Evans, in *Stochastic Networks: Theory and Applications* (Eds: F. P. Kelly, S. Zachary, I. Ziedins), Clarendon, Oxford **1996**.
- [111] P. J. Courtois, *Decomposability: Queueing and Computer System Applications*, ACM Monograph Series, Academic Press, New York **1977**.
- [112] A. E. Conway, *Queueing Networks—Exact Computational Algorithms: A Unified Theory Based on Decomposition and Aggregation*, Computer Systems, MIT Press, Cambridge MA **1989**.
- [113] D. Tse, R. Gallager, J. Tsitsiklis, *IEEE J. Sel. Areas Commun.* **1995**, *13*, 1028.
- [114] T. J. Brereton, D. P. Kroese, O. Stenzel, V. Schmidt, B. Baumeier, *Proc. Winter Simul. Conf.*, Efficient Simulation of Charge Transport in Deep-Trap Media, IEEE, Berlin **2012**.
- [115] M. Faessel, D. Jeulin, *J. Microsc.* **2010**, *239*, 17.

- [116] S. Beucher, C. Lantuéjoul, *Proc. Int. Workshop Image Process., Real-Time Edge Motion Detect./Estimat. Use of Watersheds in Contour Detection*, Rennes **1979**, pp. 2.1–2.12.
- [117] S. Beucher, F. Meyer, *Opt. Eng.* **1993**, *34*, 433.
- [118] H. Choi, D. B. Szyld, *Proc. IEEE Int. Comput. Perform. Dependability Symp. Application of Threshold Partitioning of Sparse Matrices to Markov Chains*, IEEE, Urbana, IL **1996**, pp. 158–165.
- [119] T. H. Cormen, S. Clifford, C. E. Leiserson, R. L. Rivest, *Introduction to Algorithms*, MIT Electrical Engineering and Computer Science, MIT Press, Cambridge, MA **1990**.
- [120] Y. Roichman, N. Tessler, *Appl. Phys. Lett.* **2002**, *80*, 1948.
- [121] P. R. Emtage, J. J. O'Dwyer, *Phys. Rev. Lett.* **1966**, *16*, 356.
- [122] S. L. M. van Mensfoort, R. Coehoorn, *Phys. Rev. B* **2008**, *78*, 085207.
- [123] E. Tutiš, I. Batistić, D. Berner, *Phys. Rev. B* **2004**, *70*, 161202.
- [124] K. Meisel, W. Pasveer, J. Cottaar, C. Tanase, R. Coehoorn, P. Bobbert, P. Blom, D. de Leeuw, M. Michels, *Phys. Status Solidi C* **2006**, *3*, 267.
- [125] N. Rappaport, Y. Preezant, N. Tessler, *Phys. Rev. B* **2007**, *76*, 235323.
- [126] J. J. M. van der Holst, M. A. Uijtewaai, B. Ramachandhran, R. Coehoorn, P. A. Bobbert, G. A. de Wijs, R. A. de Groot, *Phys. Rev. B* **2009**, *79*, 085203.
- [127] S. V. Novikov, G. G. Malliaras, *Phys. Rev. B* **2006**, *73*, 033308.
- [128] M. A. Lampert, *Current Injection in Solids*, Electrical Science, Academic Press, New York **1970**.
- [129] W. Gao, A. Kahn, *J. Phys.: Condens. Matter* **2003**, *15*, S2757.
- [130] M. Kröger, S. Hamwi, J. Meyer, T. Riedl, W. Kowalsky, A. Kahn, *Appl. Phys. Lett.* **2009**, *95*, 123301.
- [131] P. Erk, M. Bold, M. Egen, E. Fuchs, T. Geßner, K. Kahle, C. Lennartz, O. Molt, S. Nord, H. Reichelt, C. Schildknecht, H.-H. Johannes, W. Kowalsky, *SID Symp. Digest Technical Papers* **2006**, *37*, 131.
- [132] M. M. Rothmann, S. Haneder, E. Da Como, C. Lennartz, C. Schildknecht, P. Strohriegl, *Chem. Mater.* **2010**, *22*, 2403.
- [133] M. M. Rothmann, E. Fuchs, C. Schildknecht, N. Langer, C. Lennartz, I. Münster, P. Strohriegl, *Org. Electron.* **2011**, *12*, 1192.
- [134] D. Wagner, Rothmann, M. Strohriegl, P. Lennartz, C. Münster, I. Wagenblast, G. Schildknecht, *Proc. SPIE* **2012**, *9*, 847610.
- [135] A. Klamt, G. Schüürmann, *J. Chem. Soc., Perkin Trans. 2* **1993**, 799.
- [136] C. Adachi, M. A. Baldo, S. R. Forrest, M. E. Thompson, *Appl. Phys. Lett.* **2000**, *77*, 904.
- [137] V. I. Adamovich, S. R. Cordero, P. I. Djurovich, A. Tamayo, M. E. Thompson, B. W. D'Andrade, S. R. Forrest, *Org. Electron.* **2003**, *4*, 77.
- [138] M. A. Baldo, S. Lamansky, P. E. Burrows, M. E. Thompson, S. R. Forrest, *Appl. Phys. Lett.* **1999**, *75*, 4.
- [139] S. Lamansky, P. Djurovich, D. Murphy, F. Abdel-Razzaq, H.-E. Lee, C. Adachi, P. E. Burrows, S. R. Forrest, M. E. Thompson, *J. Am. Chem. Soc.* **2001**, *123*, 4304.
- [140] H. Gao, C. Qin, H. Zhang, S. Wu, Z.-M. Su, Y. Wang, *J. Phys. Chem. A* **2008**, *112*, 9097.
- [141] A. P. Kulkarni, C. J. Tonzola, A. Babel, S. A. Jenekhe, *Chem. Mater.* **2004**, *16*, 4556.
- [142] R. S. Deshpande, V. Bulović, S. R. Forrest, *Appl. Phys. Lett.* **1999**, *75*, 888.
- [143] J.-W. Kang, D.-S. Lee, H.-D. Park, J. W. Kim, W.-I. Jeong, Y.-S. Park, S.-H. Lee, K. Go, J.-S. Lee, J.-J. Kim, *Org. Electron.* **2008**, *9*, 452.
- [144] S. A. V. Slyke, C. H. Chen, C. W. Tang, *Appl. Phys. Lett.* **1996**, *69*, 2160.
- [145] K. S. Son, M. Yahiro, T. Imai, H. Yoshizaki, C. Adachi, *Chem. Mater.* **2008**, *20*, 4439.
- [146] Q. Wang, J. Ding, Z. Zhang, D. Ma, Y. Cheng, L. Wang, F. Wang, *J. Appl. Phys.* **2009**, *105*, 076101.
- [147] Y. Kijima, N. Asai, S.-i. Tamura, *Jpn. J. Appl. Phys.* **1999**, *38*, 5274.
- [148] T. Tsuji, S. Naka, H. Okada, H. Onnagawa, *Appl. Phys. Lett.* **2002**, *81*, 3329.
- [149] R. Meerheim, S. Scholz, S. Olthof, G. Schwartz, S. Reineke, K. Walzer, K. Leo, *J. Appl. Phys.* **2008**, *104*, 014510.
- [150] K. O. Cheon, J. Shinar, *Appl. Phys. Lett.* **2002**, *81*, 1738.
- [151] P. Niyamakom, *Ph.D. Thesis*, RWTH Aachen University, **2008**.
- [152] P. Friederich, F. Symalla, V. Meded, T. Neumann, W. Wenzel, *J. Chem. Theory Comput.* **2014**, *10*, 3720.
- [153] S. L. M. V. Mensfoort, V. Shabro, R. J. D. Vries, R. A. J. Janssen, R. Coehoorn, *J. Appl. Phys.* **2010**, *107*, 113710.
- [154] C. W. Tang, S. A. VanSlyke, *Appl. Phys. Lett.* **1987**, *51*, 913.
- [155] G. G. Malliaras, Y. Shen, D. H. Dunlap, H. Murata, Z. H. Kafafi, *Appl. Phys. Lett.* **2001**, *79*, 2582.
- [156] C. H. M. Marée, R. A. Weller, L. C. Feldman, K. Pakbaz, H. W. H. Lee, *J. Appl. Phys.* **1998**, *84*, 4013.